SANDIA REPORT

SAND2007-1423
Unlimited Release
Printed March 2007

A Multi-Scale Q1/P0 Approach to Lagrangian Shock Hydrodynamics

Guglielmo Scovazzi, Edward Love, and Mikhail Shashkov

Sandia National Laboratories

A Multi-Scale Q1/P0 Approach to Lagrangian Shock Hydrodynamics

Guglielmo Scovazzi
1431 Computational Shock- and Multi-physics Department
Sandia National Laboratories
P.O. Box 5800, MS 1319
Albuquerque, NM 87185-1319, USA
gscovaz@sandia.gov

Edward Love
1431 Computational Shock- and Multi-physics Department
Sandia National Laboratories
P.O. Box 5800, MS 1319
Albuquerque, NM 87185-1319, USA
elove@sandia.gov

Mikhail J. Shashkov
Theoretical Division, Group T-7, MS B284
Los Alamos National Laboratory
Los Alamos, NM 87545, USA
shashkov@lanl.gov

Abstract

A new multi-scale, stabilized method for Q1/P0 finite element computations of Lagrangian shock hydrodynamics is presented. Instabilities (of hourglass type) are controlled by a stabilizing operator derived using the variational multi-scale analysis paradigm. The resulting stabilizing term takes the form of a pressure correction. With respect to currently implemented hourglass control approaches, the novelty of the method resides in its residual-based character. The stabilizing residual has a definite physical meaning, since it embeds a discrete form of the Clausius-Duhem inequality. Effectively, the proposed stabilization samples and acts to counter the production of entropy due to numerical instabilities. The proposed technique is applicable to materials with no shear strength, for which there exists a caloric equation of state. The stabilization operator is incorporated into a mid-point, predictor/multi-corrector time integration algorithm, which conserves mass, momentum and total energy. Encouraging numerical results in the context of compressible gas dynamics confirm the potential of the method.

Acknowledgments

Contents

A Multi-Scale Q1/P0 Approach to Lagrangian Shock Hydrodynamics

1 Introduction

In [31, 30], a multi-scale approach was applied in finite element computations of Lagrangian shock hydrodynamics. In that case, a piece-wise linear, continuous approximation in space was adopted for all the solution variables.

Given the encouraging results of the approach in [31], extensions to the case of Q1/P0 finite element are investigated in the present work. Q1/P0 refers to the piece-wise linear, continuous approximation of the kinematic variables (position/displacement, velocity, acceleration), and the piece-wise constant, discontinuous approximation of the thermodynamic variables (density, pressure, internal energy).

Among the requirements in developing a consistent formulation, conservation of mass, momentum and total energy are considered essential. In addition, a straightforward definition of the total energy of the system is also considered very important. In fact, most of the finite element implementations for shock hydrodynamics leverage a central difference time integrator in which displacements, velocities and accelerations are collocated in time according to a staggered approach (see, e.g., [5] for a review of the state of the practice). Although very efficient in terms of storage and computational cost, such central difference implementations suffer from a cumbersome definition of the kinetic energy, which involves the product of algorithmic velocities at two different time instants. This is seen as a problem by the authors, since, by definition, the algorithmic kinetic energy is not ensured to be positive [5].

The present paper proposes an alternative approach, in which a mid-point type integrator is implemented by means of a conservative predictor/multi-corrector procedure. Thanks to this approach, a straightforward definition of the total energy is obtained. To the authors' best knowledge, the proposed algorithm is new in finite element hydrocode implementations, although a similar approach was originally proposed by Caramana, Shashkov and Whalen [6], in the context of mimetic finite differences. The proposed approach also shares significant similarities with the space-time integrators discussed in [31].

At the core of the algorithm is a novel, multi-scale operator which controls hourglass-type instabilities. Applying the multi-scale analysis [18, 19] to the base Galerkin formulation shows how instabilities can be controlled. For materials with no shear strength (e.g., fluids) the stabilization takes the form of a *pressure enrichment*, ultimately dependent on the *residual* of a rate equation for the pressure. The residual character of the stabilization preserves the consistency of the method, and, at the same time, reveals important connections between numerical instabilities and physical aspects of the problem simulated. In fact, the pressure equation residual can be interpreted as a statement of the Clausius-Duhem entropy inequality. Effectively, the pressure residual *samples* and *counters* the production of entropy due to numerical instabilities. Previous work has gone in the direction of *physical hourglass control design* [2, 3, 29]: The present work takes an even closer look at the interplay between physical consistency and numerical instabilities of algorithms.

One very important point is that the multi-scale stabilization operator, when applied to a three-dimensional, compressible, inviscid flow, acts only on the hourglass modes which are not divergence-free. This should not be surprising, since, *per se*, the material has no shear strength, and, therefore, there cannot be any residual equation providing shear resistance. However, divergence-free modes associated

with *non-homogeneous deviatoric motion* (shear) are an integral part of the hourglass eigenspace.

The multi-scale approach enables a clear delineation of the true *dilemma* faced by the analyst when using Q1/P0 finite elements formulations for fluid flow computations. On the one hand, any attempt to include artificial shear strength in the fluid may negatively affect the quality of the simulation. On the other hand, three-dimensional computations may be unstable if non-homogeneous shear modes are undamped. This fact is considered by the authors not as a shortcoming of the multi-scale approach, but rather as a fundamental flaw of Q1/P0 formulations for inviscid fluids.

In order to stabilize the non-homogeneous shear modes, an artificial viscosity acting on the fluctuation of the deviatoric part of the symmetric velocity gradient is introduced. This correction term does not perturb the convergence rates of the method, since it acts to damp the difference between the deviator of the symmetric gradient of the velocity and its element-average. Contrary to all other examples of hourglass control techniques for fluids, the multi-scale analysis shows that the stabilization operators for non-homogeneous shear modes can be designed in a completely autonomous way with respect to the control of hourglass modes which are not divergence-free. The multi-scale approach provides therefore a *new* perspective on an *old* problem, posing a clear boundary between what can be stabilized on physical grounds, and what has to be stabilized with purely artificial mechanisms. It is also of interest that in the vast literature of SUPG methods (see, e.g., [25, 22, 21, 20, 14, 15, 16, 27, 33, 37, 36, 41, 42, 38, 39, 40] and references therein) no hourglass instabilities of shear type were ever observed. Further investigation on this subject is in our opinion required, to fully evaluate whether or not standard SUPG methods on piecewise linear approximations necessitate "deviatoric" stabilization when applied to Lagrangian or Eulerian computations of inviscid flows.

An integral part of the proposed approach is the shock-capturing operator, in the form of an artificial stress tensor, based on the symmetric part of the velocity gradient. This choice, , already explored in [31], yields an *objective* stress tensor, which proves superior to standard artificial viscosity operators, constructed with the velocity divergence. Whenever spurious *homogeneous shear* modes are generated across the shock layer, the tensor viscosity delivers much improved results, from both the accuracy and robustness standpoints. In particular, improvements with respect to [31] on the selection of the length scale in the artificial viscosity are discussed.

The rest of the exposition is organized as follows: The basic equations of Lagrangian hydrodynamics are introduced in Section 2. The variational formulation is established in Section 3, and the time-integration algorithm is described in Section 4. Section 5 is devoted to the multi-scale analysis and design of the multi-scale hourglass stabilization. The shock-capturing operator is described in Section 6. Section 7 contains additional comments on the implementation of the algorithm, the integration quadratures used, and the time step CFL constraints for the method. Results of the numerical tests are analyzed in Section 8. Conclusions and future research perspectives are summarized in Section 9.

2 Equations of Lagrangian shock hydrodynamics

The equations of Lagrangian shock hydrodynamics express the changes in position, momentum and total energy of a compressible body of fluid, as it deforms. Let Ω_0 and Ω be open sets in $\mathbb{R}^{n_d}$ (where n_d is the number of spatial dimensions). The *deformation*

$$\varphi : \Omega_0 \rightarrow \Omega = \varphi(\Omega_0) , \tag{1}$$

$$\boldsymbol{X} \mapsto \boldsymbol{x} = \varphi(\boldsymbol{X}, t) , \quad \forall \boldsymbol{X} \in \Omega_0, \ t \geq 0 , \tag{2}$$
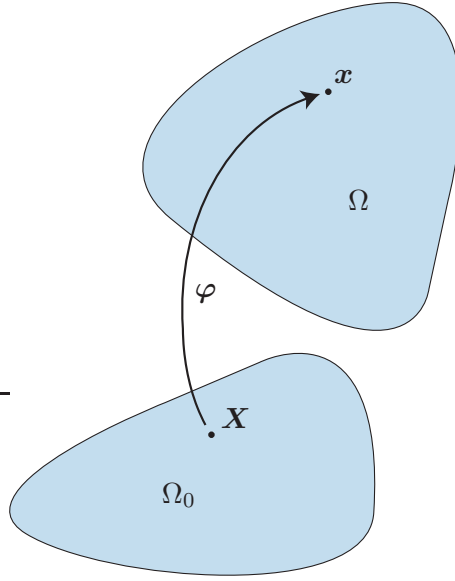
Figure 1. Sketch of the Lagrangian map $\boldsymbol{\varphi}$.

is the mapping from the original to the current configuration of the material. Here $\boldsymbol{X}$ is the material coordinate, representing the initial position of an infinitesimal material particle of the body, and $\boldsymbol{x}$ is the position of that particle in the current configuration (see Fig. 1). Ω_0 is the domain occupied by the body in its initial configuration, with boundary Γ_0. $\boldsymbol{\varphi}$ maps Ω_0 to Ω, the domain occupied by the body in its current configuration, with boundary Γ. It is also useful to define the *deformation gradient*, and the *deformation Jacobian determinant*:

$$\boldsymbol{F} = \nabla_{\mathbf{X}}\,\boldsymbol{\varphi} = \frac{\partial \varphi_i}{\partial X_j} = \frac{\partial x_i}{\partial X_j}\ , \tag{3}$$

$$J = \det(\boldsymbol{F})\ . \tag{4}$$

On a domain Ω in the current configuration, the conservative form of the equations of Lagrangian hydrodynamics, consisting of mass, momentum and energy, can be formulated as follows:

$$\rho\,J = \rho_0\ , \tag{5}$$

$$\rho\,\dot{\boldsymbol{v}} = \rho\,\boldsymbol{g} + \nabla_{\boldsymbol{x}}\!\cdot\boldsymbol{\sigma}\ , \tag{6}$$

$$\rho\,\dot{E} = \rho\,\boldsymbol{g}\cdot\boldsymbol{v} + \rho\,r + \nabla_{\boldsymbol{x}}\!\cdot(\boldsymbol{\sigma}^T\boldsymbol{v} + \boldsymbol{q})\ , \tag{7}$$

$$\dot{\boldsymbol{u}} = \boldsymbol{v}\ . \tag{8}$$

Here, $\nabla_{\boldsymbol{x}}$ and $\nabla_{\boldsymbol{x}}\!\cdot$ are the current configuration gradient and divergence operators, and $\dot{(\cdot)}$ indicates the material, or Lagrangian time derivative. $\boldsymbol{u} = \boldsymbol{x} - \boldsymbol{X}$ is the displacement vector, ρ_0 is the reference (initial) density, ρ is the (current) density, $\boldsymbol{v}$ is the velocity, $\boldsymbol{g}$ is the body force, $\boldsymbol{\sigma}$ is the Cauchy stress (a symmetric tensor), $E = \epsilon + \boldsymbol{v}\cdot\boldsymbol{v}/2$ is the total energy, the sum of the internal energy e and the kinetic energy $\boldsymbol{v}\cdot\boldsymbol{v}/2$, r is the energy source term, and $\boldsymbol{q}$ is the heat flux. E, ϵ, $\boldsymbol{g}$, r are measured per unit mass.

Remarks

1. Equations (6) and (7) are in Lagrangian *conservative* (or divergence) form. In fact, the Lagrangian

9

rate of change of an intensive, scalar variable ϕ is given by

$$\frac{\mathrm{d}}{\mathrm{d}t} \int_\Omega \rho\phi \ \mathrm{d}\Omega = \frac{\mathrm{d}}{\mathrm{d}t} \int_\Omega \rho_0\phi \ \mathrm{d}\Omega_0 = \int_\Omega \rho_0\dot\phi \ \mathrm{d}\Omega_0 = \int_\Omega \rho\dot\phi \ \mathrm{d}\Omega \ , \tag{9}$$

where (5) has been used, together with the identity

$$\rho_0 \ \mathrm{d}\Omega_0 = \rho J \ \mathrm{d}\Omega_0 = \rho \ \mathrm{d}\Omega \ . \tag{10}$$

2. The kinetic energy equation, the inner product of (6) and the velocity vector field, can be subtracted from equation (7), yielding

$$\rho\dot\epsilon = \rho \ r + \nabla_x v : \sigma + \nabla_x \cdot q \ , \tag{11}$$

where, in index notation, $\sigma^T : \nabla_x v = \sigma_{ji} \ \partial_{x_i} v_j$, and $\nabla_x v : \sigma = \sigma : \nabla_x v = \sigma^T : \nabla_x v$, since σ is symmetric. Clearly (11) is not in conservative form. However, it will be possible to use this equation in appropriate variational formulations maintaining global conservation properties (see Section 4).

The system of equations (5)–(8) has to be complemented with appropriate boundary conditions. Assuming that the boundary $\Gamma = \partial\Omega$ is partitioned as $\Gamma = \overline{\Gamma^g \cup \Gamma^h}$, $\Gamma^g \cap \Gamma^h = \emptyset$, *displacement boundary conditions* are applied on Γ^g, the *Dirichlet* boundary, and *traction boundary conditions* are applied on Γ^h, the *Neumann* boundary. Namely,

$$u|_{\Gamma^g} = u_{bc}(x,t) \ , \tag{12}$$
$$\sigma n|_{\Gamma^h} = t(x,t) \ . \tag{13}$$

Equations (5)–(8) and boundary conditions (12)-(13) completely defines the evolution of the system, once initial conditions are specified.

2.1 Constitutive laws

The analysis presented in what follows is specific to materials with no deformation strength. In this case, the Cauchy stress σ reduces to an isotropic tensor, dependent only on the thermodynamic pressure:

$$\sigma = -p I_{n_d \times n_d} \ , \tag{14}$$

or, in index notation,

$$\sigma_{ij} = -p \ \delta_{ij} \ , \tag{15}$$

with δ_{ij} the Kronecker tensor. An equation of state of the type

$$p = \hat{p}(\rho, \epsilon) \ , \tag{16}$$

is assumed. Equations of state of Mie-Grüneisen type are compatible with (16), namely

$$\hat{p}(\rho, \epsilon) = f_1(\rho) + f_2(\rho)\epsilon \ , \tag{17}$$

and apply to materials such as compressible ideal gases, co-volume gases, high explosives, and elastic-plastic solids with no strength (a situation that can be achieved when bulk stresses in the material are larger than shear stresses by orders of magnitude). For example, ideal gases satisfy (17), with $f_1 = 0$ and $f_2 = (\gamma - 1)\rho$, to yield

$$\hat{p}(\rho, \epsilon) = (\gamma - 1)\rho\epsilon \ . \tag{18}$$

3   Variational formulation of Lagrangian hydrodynamics

Finite element approximations leverage a variational statement of the equations of motion. The first step in the development of a variational form for (5), (6), (7) (or, (11)), and (8), is to define the (variational) *trial* spaces for the kinematic and thermodynamic variables, which characterize the *state* of the system. In particular, $\mathcal{S}_\kappa$ denotes the space of admissible displacements, or more generally, the space of admissible values for the kinematic variables (displacements, velocities, accelerations). Analogously, $\mathcal{S}_\gamma$ is the space of admissible thermodynamic states. Specific discrete definitions of $\mathcal{S}_\kappa$ and $\mathcal{S}_\gamma$ are given in the next section, where the discrete form of the variational equations is presented. For now, it is important to observe that the space $\mathcal{S}_\kappa$ incorporates the set of *essential* boundary conditions (12), that is, boundary conditions of kinematic (Dirichlet) type are imposed *strongly*. In addition, *test* spaces can be defined: $\mathcal{V}_\kappa$ is the space of variations – compatible with (12) – for the kinematic variables, and $\mathcal{V}_\gamma$ is the space of variations for the thermodynamic variables. Using (9) and (10), the variational problem associated with (5), (6), (11) reads:

Find $\rho \in \mathcal{S}_\gamma$, $\boldsymbol{v} \in \mathcal{S}_\kappa$, and $\epsilon \in \mathcal{S}_\gamma$, such that, $\forall \psi_\gamma \in \mathcal{V}_\gamma$, and $\forall \boldsymbol{\psi}_\kappa \in \mathcal{V}_\kappa$,

$$0 = \int_{\Omega_0} \psi_\gamma \left(\rho_0 - \rho J \right) \, \mathrm{d}\Omega_0 \,, \tag{19}$$

$$0 = \int_{\Omega_0} \boldsymbol{\psi}_\kappa \cdot (\rho_0 \dot{\boldsymbol{v}}) \, \mathrm{d}\Omega_0 + \int_\Omega \nabla_{\boldsymbol{x}}^s \boldsymbol{\psi}_\kappa : \boldsymbol{\sigma} \, \mathrm{d}\Omega - \int_{\Gamma^h} \boldsymbol{\psi}_\kappa \cdot \boldsymbol{t} \, \mathrm{d}\Gamma - \int_\Omega \boldsymbol{\psi}_\kappa \cdot (\rho \boldsymbol{g}) \, \mathrm{d}\Omega \,, \tag{20}$$

$$0 = \int_{\Omega_0} \psi_\gamma \left(\rho_0 \dot{\epsilon} \right) \, \mathrm{d}\Omega_0 - \int_\Omega \psi_\gamma \left(\nabla_{\boldsymbol{x}}^s \boldsymbol{v} : \boldsymbol{\sigma} + \nabla_{\boldsymbol{x}} \cdot \boldsymbol{q} + \rho r \right) \, \mathrm{d}\Omega \,, \tag{21}$$

where $\nabla_{\boldsymbol{x}}^s = 1/2(\nabla_{\boldsymbol{x}}{}^T + \nabla_{\boldsymbol{x}})$ is the symmetric part of the gradient operator, and $\nabla_{\boldsymbol{x}} \boldsymbol{v} : \boldsymbol{\sigma} = \nabla_{\boldsymbol{x}}^s \boldsymbol{v} : \boldsymbol{\sigma}$, since $\boldsymbol{\sigma}$ is symmetric. Notice that the traction (or, *natural*) boundary conditions are imposed in (20) through the weak form.

4   Time integration and discrete weak forms

The variational form of the Lagrangian hydrodynamics equations and its conservation properties are strictly related to the choice of time-integration algorithm. In the present work, a mid-point type integration scheme is adopted, which, in combination with an appropriate predictor/corrector solution strategy, yields an explicit iterative algorithm. The proposed formulation conserves mass, momentum and total energy, without resorting to any staggered approach in time, with striking analogies to the space-time integration presented in [31]. A similar approach is usually adopted in the context of *mimetic* or *compatible* discretizations [6].

4.1   Test and trial spaces

In terms of the spatial discretization, the proposed approach is no different from standard Lagrangian hydrodynamic finite element methods [5, 13]. Kinematic variables are approximated by piecewise-linear, continuous functions (node-centered degrees-of-freedom), and all thermodynamic variables are approximated by piecewise-constant, discontinuous functions (cell-centered degrees-of-freedom). Consequently, the test-space for the momentum equation consists of piecewise-linear, continuous functions, while the test space for the mass and energy equations is given by the piecewise-constant, discontinuous functions. The

trial function spaces $\mathcal{S}^h$ and test function spaces $\mathcal{V}^h$ are then given by:

$$\mathcal{S}^h_\kappa = \left\{ \boldsymbol{\psi}_\kappa \in (C^0(\Omega))^{n_d} : \boldsymbol{\psi}^h_\kappa \big|_{\Omega_e} \in (\mathcal{P}_1(\Omega_e))^{n_d}, \boldsymbol{\psi}^h_\kappa = \boldsymbol{g}_{bc}(t) \text{ on } \Gamma^g \right\} , \tag{22}$$

$$\mathcal{V}^h_\kappa = \left\{ \boldsymbol{\psi}_\kappa \in (C^0(\Omega))^{n_d} : \boldsymbol{\psi}^h_\kappa \big|_{\Omega_e} \in (\mathcal{P}_1(\Omega_e))^{n_d}, \boldsymbol{\psi}^h_\kappa = \boldsymbol{0} \text{ on } \Gamma^g \right\} , \tag{23}$$

$$\mathcal{S}^h_\gamma = \left\{ \psi^h_\gamma \in L^2(\Omega) : \boldsymbol{\psi}^h_\gamma \big|_{\Omega_e} \in \mathcal{P}^0(\Omega_e), \right\} , \tag{24}$$

$$\mathcal{V}^h_\gamma = \mathcal{S}^h_\gamma , \tag{25}$$

where $\boldsymbol{g}_{bc}(t)$ indicates the essential (Dirichlet) boundary conditions, possibly dependent on time.

4.2 Variational equations

The momentum and energy balances are considered first. For the sake of simplicity, it is assumed that body forces, heat fluxes and heat sources are absent. The time step is indicated by Δt, and the mid-point value of a quantity f is defined as:

$$f_{n+1/2} = \frac{f_n + f_{n+1}}{2} . \tag{26}$$

4.2.1 Momentum balance

Find $\boldsymbol{v} \in \mathcal{S}^h_\kappa$, such that, $\forall \boldsymbol{\psi}^h_\kappa \in \mathcal{V}^h$,

$$\int_{\Omega_0} \boldsymbol{\psi}^h_\kappa \cdot \rho_0 \left(\boldsymbol{v}_{n+1} - \boldsymbol{v}_n \right) \mathrm{d}\Omega_0$$
$$+ \Delta t \int_{\Omega_{n+1/2}} (\nabla_{\boldsymbol{x}} \boldsymbol{\psi}^h_\kappa)_{n+1/2} : \tilde{\boldsymbol{\sigma}}_{n+1/2} \, \mathrm{d}\Omega - \Delta t \int_{\Gamma^h_{n+1/2}} \boldsymbol{\psi}^h_\kappa \cdot \boldsymbol{t}_{n+1/2} \, \mathrm{d}\Gamma = 0 , \tag{27}$$

where $\nabla_{\boldsymbol{x}}$ is the current configuration gradient operator. Notice the slight abuse of notation, since the superscript "h", indicating spatial discretization, should be applied to all solution variables, discrete gradient operators, and the domain geometry. This is avoided whenever possible, to favor a simpler presentation of algebraic expressions. Notice that the physical traction $\boldsymbol{t}$ acts only on the Neumann boundary (i.e., $\boldsymbol{t}|_{\Gamma^g} = 0$), and the notation $\tilde{\boldsymbol{\sigma}}$ indicates an algorithmic stress, whose general expression is

$$\tilde{\boldsymbol{\sigma}} = \boldsymbol{\sigma} + \boldsymbol{\sigma}_{vms} + \boldsymbol{\sigma}_{art} , \tag{28}$$

where $\boldsymbol{\sigma}_{vms}$ is the multi-scale, residual-based stress tensor, designed to control hourglass instabilities, and $\boldsymbol{\sigma}_{art}$ is the artificial viscosity stress tensor, designed to capture shock layers.

It is usual practice in hydrodynamic computations to *lump* the mass matrix in the momentum equation, to avoid any matrix inversions in the solution procedure. The velocity field at time $t_\bullet$ is interpolated as

$$\boldsymbol{v}_\bullet = \sum_{B=1}^{n_{np}} N^B(\boldsymbol{X}) \mathsf{v}_{\bullet;B} . \tag{29}$$

Here $\mathbf{v}_{\bullet;B}$ and $N^B(\boldsymbol{X})$ are the n_d-dimensional vector of velocity degrees-of-freedom and the shape function, both associated with node B, and n_{np} is the number of nodes in the computational mesh. The mass lumping is achieved applying the following approximation (no index sum is implied unless expressly stated):

$$
\begin{aligned}
\int_{\Omega_\bullet} N^A(\boldsymbol{X})\,(\rho v_i)_\bullet\,\mathrm{d}\Omega &= \int_{\Omega_0} N^A(\boldsymbol{X})\rho_0(v_i)_\bullet\,\mathrm{d}\Omega_0 \\
&= \sum_{B=1}^{n_{np}} \left(\int_{\Omega_0} N^A(\boldsymbol{X})N^B(\boldsymbol{X})\rho_0\,\mathrm{d}\Omega_0 \right) (\mathsf{v}_i)_{\bullet;B} \\
&\approx \sum_{B=1}^{n_{np}} \left(\int_{\Omega_0} N^A(\boldsymbol{X})\,\delta^{AB}\,\rho_0\,\mathrm{d}\Omega_0 \right) (\mathsf{v}_i)_{\bullet;B} \\
&= \mathcal{M}_L^A\,(\mathsf{v}_i)_{\bullet;A}\,,
\end{aligned}
\tag{30}
$$

where v_i and v_i are the ith components of $\boldsymbol{v}$ and $\mathbf{v}$, respectively, $A = 1, 2, \ldots, n_{np}$, δ^{AB} is the Kronecker symbol, and

$$
\mathcal{M}_L^A = \int_{\Omega_0} N^A(\boldsymbol{X})\rho_0\,\mathrm{d}\Omega_0
\tag{31}
$$

is the the mass associated to node A in the global numbering. Defining

$$
[\mathbf{M}_L] = [\mathrm{diag}\{\{\mathcal{M}_L^A, \mathcal{M}_L^A, \mathcal{M}_L^A\}^T\}]\,,
\tag{32}
$$

$$
\mathbf{F}_{n+1/2} = \{\mathbf{F}_{n+1/2;A}\}\,,
\tag{33}
$$

$$
\mathbf{F}_{n+1/2;A} = \int_{\Omega_{n+1/2}} \tilde{\boldsymbol{\sigma}}_{n+1/2}(\nabla_x N^A)_{n+1/2}\,\mathrm{d}\Omega - \int_{\Gamma_{n+1/2}} N^A \tilde{\boldsymbol{t}}_{n+1/2}\,\mathrm{d}\Gamma\,,
\tag{34}
$$

where $[\mathbf{M}_L]$ is a diagonal $[(n_d \times n_{np}) \times (n_d \times n_{np})]$-matrix and $\mathbf{F}_{n+1/2}$ is a $(n_d \times n_{np})$-vector, equation (27) reduces to

$$
[\mathbf{M}_L]\,(\mathbf{v}_{n+1} - \mathbf{v}_n) + \Delta t\,\mathbf{F}_{n+1/2} = 0\,.
\tag{35}
$$

4.2.2 Energy balance

Integrating in time (21), yields:

    Find $\epsilon \in \mathcal{S}_\gamma^h$, such that, $\forall \psi_\gamma^h \in \mathcal{V}^h$,

$$
\int_{\Omega_0} \psi_\gamma^h \rho_0\,(\epsilon_{n+1} - \epsilon_n)\,\mathrm{d}\Omega_0 - \Delta t \int_{\Omega_{n+1/2}} \psi_\gamma^h\,(\nabla_x \boldsymbol{v})_{n+1/2} : \tilde{\boldsymbol{\sigma}}_{n+1/2}\,\mathrm{d}\Omega = 0\,.
\tag{36}
$$

Recalling that ψ_γ, ϵ, and ρ are constant over each element, one can introduce the following definitions:

$$
[\mathbf{M}_{el}] = [\mathrm{diag}\{\mathbf{M}_{el}\}]\,,
\tag{37}
$$

$$
\mathbf{M}_{el} = \{\mathcal{M}_e\}\,,
\tag{38}
$$

$$
\mathcal{M}_e = \int_{\Omega_{\bullet;e}} \rho_\bullet\,\mathrm{d}\Omega = \int_{\Omega_{0;e}} \rho_0\,\mathrm{d}\Omega_0\,.
\tag{39}
$$

$$
\mathbf{W}_{n+1/2} = \{\mathsf{W}_{n+1/2;e}\}\,,
\tag{40}
$$

$$
\mathsf{W}_{n+1/2;e} = \left\{ -\int_{\Omega_{n+1/2;e}} (\nabla_x \boldsymbol{v})_{n+1/2} : \tilde{\boldsymbol{\sigma}}_{n+1/2}\,\mathrm{d}\Omega \right\}\,,
\tag{41}
$$

$$
\tag{42}
$$

13

where $\Omega_{\bullet;e}$ is the element domain at time $t_\bullet$, $\mathbf{M}_{el}$ and $\mathbf{W}_{n+1/2}$ are n_{el}-dimensional vectors, and n_{el} is the number of elements in the computational list. Then, equation (36) reduces to

$$[\mathbf{M}_{el}]\,(\boldsymbol{\epsilon}_{n+1} - \boldsymbol{\epsilon}_n) + \Delta t\,\mathbf{W}_{n+1/2} = \mathbf{0}\;. \tag{43}$$

where $\boldsymbol{\epsilon}_\bullet$ is the vector of cell-centered degrees-of-freedom for the internal energy ϵ at time $t_\bullet$.

4.2.3 Mass balance

The mass conservation equation (19) can be slightly rearranged to yield:

$\quad$ *Find* $\rho \in \mathcal{S}_\gamma^h$, *such that,* $\forall \psi_\gamma^h \in \mathcal{V}^h$,

$$\int_{\Omega_0} \psi_\gamma^h \rho_0\,\mathrm{d}\Omega_0 = \int_{\Omega_0} \psi_\gamma^h \rho J\,\mathrm{d}\Omega_0 = \int_\Omega \psi_\gamma^h \rho\,\mathrm{d}\Omega\;. \tag{44}$$

Integrating the previous equation element-by-element results in

$$\mathbf{M}_{el} = [\mathbf{V}_\bullet]\boldsymbol{\rho}_\bullet\;, \tag{45}$$

where

$$\boldsymbol{\rho}_\bullet = \{\rho_{\bullet;e}\}\;, \tag{46}$$

$$[\mathbf{V}_\bullet] = [\mathrm{diag}\{\mathbf{V}_\bullet\}]\;, \tag{47}$$

$$\mathbf{V}_\bullet = \{\mathsf{V}_{\bullet;e}\}\;, \tag{48}$$

$$\mathsf{V}_{\bullet;e} = \int_{\Omega_{0;e}} J_\bullet\,\mathrm{d}\Omega_0 = \mathrm{meas}(\Omega_{\bullet;e})\;. \tag{49}$$

4.2.4 Displacement equations

The time-discretization of the rate equations for the position field

$$\boldsymbol{x}_{n+1} - \boldsymbol{x}_n - \Delta t\,\boldsymbol{v}_{n+1/2} = \mathbf{0} \tag{50}$$

yields a set of ordinary differential equations for the nodal positions, namely

$$\mathbf{x}_{n+1} - \mathbf{x}_n - \Delta t\,\mathbf{v}_{n+1/2} = \mathbf{0}\;. \tag{51}$$

4.2.5 Equation of state

The equation of state can be applied at each time step to obtain the pressure (or, in general, the stress field),

$$\boldsymbol{\sigma}_{n+1} = -p_{n+1}\boldsymbol{I} = -\hat{p}(\rho_{n+1}, \epsilon_{n+1})\boldsymbol{I}\;. \tag{52}$$

Expressing (52) in terms of the cell-centered degrees-of-freedom, one obtains

$$\mathbf{p}_{n+1} = \hat{\mathbf{p}}(\boldsymbol{\rho}_{n+1}, \boldsymbol{\epsilon}_{n+1})\;, \tag{53}$$

$$\tag{54}$$

where

$$\mathbf{p}_\bullet = \{p_{\bullet;e}\}\;, \tag{55}$$

$$\hat{\mathbf{p}}(\boldsymbol{\rho}_\bullet, \boldsymbol{\epsilon}_\bullet) = \{\hat{p}(\rho_{\bullet;e}, \epsilon_{\bullet;e})\}\;. \tag{56}$$

14

4.3 Global conservation properties

It is immediate to realize that equations (44) and (45) are statements of global and local conservation of mass, respectively. It is also evident from equation (27) or (35) that the proposed algorithm conserves the total momentum of the system. Proving conservation of total energy is somewhat less obvious, and, for this purpose, equations (27) and (36) are used. Conservation statements are usually proven in the case of homogenous Neumann boundary conditions, for which the test and trial function spaces for the velocities coincide (i.e., $\mathcal{S}_\kappa^h = \mathcal{V}_\kappa^h$). Evaluating the sum over all the nodes of (27), with $\boldsymbol{\psi}_\kappa^h = \boldsymbol{v}_{n+1/2}$, the kinetic energy balance for the system is obtained:

$$\frac{1}{2}\int_{\Omega_{n+1}} \rho_{n+1}(\boldsymbol{v}\cdot\boldsymbol{v})_{n+1}\,\mathrm{d}\Omega - \frac{1}{2}\int_{\Omega_n}\rho_n(\boldsymbol{v}\cdot\boldsymbol{v})_n\,\mathrm{d}\Omega = -\Delta t\int_{\Omega_{n+1/2}}(\nabla_{\boldsymbol{x}}\boldsymbol{v})_{n+1/2}:\tilde{\boldsymbol{\sigma}}_{n+1/2}\,\mathrm{d}\Omega\,, \tag{57}$$

The previous equation is derived using the following identity:

$$\int_{\Omega_0}\rho_0\boldsymbol{v}_{n+1/2}\cdot(\boldsymbol{v}_{n+1}-\boldsymbol{v}_n)\,\mathrm{d}\Omega_0 = \frac{1}{2}\int_{\Omega_0}\rho_0\left((\boldsymbol{v}\cdot\boldsymbol{v})_{n+1}-(\boldsymbol{v}\cdot\boldsymbol{v})_n\right)\,\mathrm{d}\Omega_0$$

$$= \frac{1}{2}\int_{\Omega_{n+1}}\rho_{n+1}(\boldsymbol{v}\cdot\boldsymbol{v})_{n+1}\,\mathrm{d}\Omega - \frac{1}{2}\int_{\Omega_n}\rho_n(\boldsymbol{v}\cdot\boldsymbol{v})_n\,\mathrm{d}\Omega\,. \tag{58}$$

Testing (36) with a unit constant shape function over the entire domain (i.e., $\psi_\gamma^h = 1$) yields

$$\int_{\Omega_{n+1}}(\rho\epsilon)_{n+1}\,\mathrm{d}\Omega - \int_{\Omega_n}(\rho\epsilon)_n\,\mathrm{d}\Omega = \int_{\Omega_0}\rho_0\left(\epsilon_{n+1}-\epsilon_n\right)\,\mathrm{d}\Omega_0$$

$$= \Delta t\int_{\Omega_{n+1/2}}(\nabla_{\boldsymbol{x}}\boldsymbol{v})_{n+1/2}:\tilde{\boldsymbol{\sigma}}_{n+1/2}\,\mathrm{d}\Omega\,. \tag{59}$$

By summing (57) and (59), and noticing that their right hand sides are equal and opposite, one can derive the following conservation statement for the total energy between time steps n and $n+1$:

$$\int_{\Omega_{n+1}}\rho_{n+1}\left(\frac{1}{2}(\boldsymbol{v}\cdot\boldsymbol{v})_{n+1}+\epsilon_{n+1}\right)\,\mathrm{d}\Omega = \int_{\Omega_n}\rho_n\left(\frac{1}{2}(\boldsymbol{v}\cdot\boldsymbol{v})_n+\epsilon_n\right)\,\mathrm{d}\Omega\,. \tag{60}$$

The previous derivations can be repeated in the case when mass lumping is applied. Using (35), an analogue of (57) can be derived, namely,

$$\frac{1}{2}\mathbf{v}_{n+1}^T[\mathbf{M}_L]\mathbf{v}_{n+1} - \frac{1}{2}\mathbf{v}_n^T[\mathbf{M}_L]\mathbf{v}_n = -\mathbf{v}_{n+1/2}^T\mathbf{F}_{n+1/2}\,. \tag{61}$$

Using the vector notation, (59) can be recast as (43) multiplied by $\mathbf{1}$, a n_{el}-dimensional vector whose entries are all unity, that is,

$$\mathbf{M}_{el}^T\left(\boldsymbol{\epsilon}_{n+1}-\boldsymbol{\epsilon}_n\right) = -\Delta t\,\mathbf{1}^T\mathbf{W}_{n+1/2}\,. \tag{62}$$

Finally, realizing that, by definition,

$$\mathbf{v}_{n+1/2}^T\mathbf{F}_{n+1/2} = -\mathbf{1}^T\mathbf{W}_{n+1/2}\,, \tag{63}$$

a statement of conservation of total energy analogous to (60) can be expressed as

$$\frac{1}{2}\mathbf{v}_{n+1}^T[\mathbf{M}_L]\mathbf{v}_{n+1} + \mathbf{M}_{el}^T\boldsymbol{\epsilon}_{n+1} = \frac{1}{2}\mathbf{v}_n^T[\mathbf{M}_L]\mathbf{v}_n + \mathbf{M}_{el}^T\boldsymbol{\epsilon}_n\,. \tag{64}$$

Retrieve loop parameters: n_{step}, $i_{\max}$
Initialize all variables with initial conditions
Form $[\mathbf{M}_L]$ and $\mathbf{M}_{el}$
For $n = 0, \ldots, n_{\text{step}}$ (*Time-step loop begins*)

 Set Δt (respecting the CFL condition)

 Predictor: $\mathbf{Y}_{n+1}^{(0)} = \mathbf{Y}_n$
 For $i = 0, \ldots, i_{\max} - 1$ (*Multi-corrector loop begins*)

  Assembly: $\mathbf{F}_{n+1/2}^{(i)}$
  Velocity update: $\mathbf{v}_{n+1}^{(i+1)} = \mathbf{v}_n - \Delta t [\mathbf{M}_L]^{-1} \mathbf{F}_{n+1/2}^{(i)}$

  Assembly: $\mathbf{W}_{n+1/2}^{(i,i+1)}$
  Internal energy update: $\boldsymbol{\epsilon}_{n+1}^{(i+1)} = \boldsymbol{\epsilon}_n - \Delta t \, [\mathbf{M}_{el}]^{-1} \mathbf{W}_{n+1/2}^{(i,i+1)}$

  Position update: $\mathbf{x}_{n+1}^{(i+1)} = \mathbf{x}_n + \Delta t \, \mathbf{v}_{n+1/2}^{(i+1)}$

  Volume update: $\mathbf{V}_{n+1}^{(i+1)} = \mathbf{V}(\mathbf{x}_{n+1}^{(i+1)})$

  Density update: $\boldsymbol{\rho}_{n+1}^{(i+1)} = [\mathbf{V}_{n+1}^{(i+1)}]^{-1} \mathbf{M}_{el}$

  Equation of state update: $\mathbf{p}_{n+1}^{(i+1)} = \hat{\mathbf{p}} \left(\boldsymbol{\rho}_{n+1}^{(i+1)}, \boldsymbol{\epsilon}_{n+1}^{(i+1)} \right)$

 End (*Multi-corrector loop ends*)

 Time update: $\mathbf{Y}_{n+1} = \mathbf{Y}_{n+1}^{(i_{\max})}$
End (*Time-step loop ends*)
Exit

Table 1. Outline of the predictor-multicorrector algorithm. Notice that all matrices are diagonal, so that all inverse operations are just vector divisions. Three iterations of the predictor/multi-corrector were used in the computations.

Remarks

1. Under appropriate boundary conditions, total angular momentum is also conserved. This is a direct consequence of the symmetry of the stress tensor and the use of a mid-point time integrator [35].

2. The total energy conservation statement (60) is a direct consequence of the cancellation of the right hand sides of (57) and (59), which are equal and opposite. This fact is used to derive artificial viscosity and variational multi-scale stabilization operators which preserve total energy in the system. In fact, to ensure conservation, it is sufficient that the discrete expression for the overall $\tilde{\boldsymbol{\sigma}}$ term remains the same in the momentum and energy equations.

4.4 A predictor/multi-corrector approach

The algorithm developed so far requires the inversion of a matrix, since the force and work terms are computed at the mid-point in time, and necessitate knowledge of the solution at time t_{n+1}. However, a fully explicit algorithm can be recovered by resorting to a predictor/multi-corrector approach. This section is devoted to this purpose.

A number of preliminary definitions are needed. The state of system at time $t = t_\bullet$ is defined by means of the vector $\mathbf{Y}_\bullet = [\mathbf{x}_\bullet^T, \mathbf{v}_\bullet^T, \boldsymbol{\rho}_\bullet^T, \boldsymbol{\epsilon}_\bullet^T, \mathbf{p}_\bullet^T]^T$. $\mathbf{F}_{n+1/2}^{(i)}$ indicates the evaluation of $\mathbf{F}_{n+1/2}$ using the state $\mathbf{Y}$ at iterate (i). The definition of the iterate of the work vector $\mathbf{W}_{n+1/2}$ is somewhat different:

$$\mathbf{W}_{n+1/2}^{(i,j)} = \{\mathrm{W}_{n+1/2;e}^{(i,j)}\} \,, \tag{65}$$

$$\mathrm{W}_{n+1/2;e}^{(i,j)} = \left\{\int_{\Omega_{n+1/2;e}^{(i)}} ((\nabla_{\boldsymbol{x}})_{n+1/2}^{(i)} \boldsymbol{v}_{n+1/2}^{(j)}) : \tilde{\boldsymbol{\sigma}}_{n+1/2}^{(i)} \,\mathrm{d}\Omega\right\} \,. \tag{66}$$

Here $\nabla_{\boldsymbol{x}\,n+1/2}^{(i)}$ and $\boldsymbol{v}_{n+1/2}^{(j)}$ indicate the (current configuration) gradient operator and the velocity field at $t = t_{n+1/2}$ and iterate i and j, respectively. This notation is needed to understand how conservation is enforced *at each iteration* of the predictor/multi-corrector procedure.

As it can be appreciated in Table 1, the proposed approach consists of a velocity update, followed, in the order, by internal energy, position, volume, density and pressure (or, more generally, stress) updates.

Remark (conservation of total energy)
The proposed predictor/multi-corrector approach maintains all the conservation properties of the base mid-point algorithm it is derived from. The crucial step in the design of the algorithm is to recognize that the work vector $\boldsymbol{W}_{n+1/2}^{(i,i+1)}$ in Table 1 has to be computed holding the geometry and all the terms in the integral (66) at iterate (i), with the exception of the velocity $\boldsymbol{v}_{n+1/2}$, which is evaluated using the new iterate $(i+1)$, available after the momentum equation is integrated in time. Using arguments virtually identical to the ones presented in Section 4.3, it is easy to realize that, indeed, *each iterate* of the predictor/multi-corrector conserves total energy, namely

$$\frac{1}{2}(\mathbf{v}_{n+1}^{(i+1)})^T [\mathbf{M}_L] \mathbf{v}_{n+1}^{(i+1)} + \mathbf{M}_{el}^T \boldsymbol{\epsilon}_{n+1}^{(i+1)} = \frac{1}{2}\mathbf{v}_n^T [\mathbf{M}_L] \mathbf{v}_n + \mathbf{M}_{el}^T \boldsymbol{\epsilon}_n \,, \tag{67}$$

since the following cancellation takes place:

$$(\mathbf{v}_{n+1/2}^{(i+1)})^T \mathbf{F}_{n+1/2}^i = -\mathbf{1}^T \mathbf{W}_{n+1/2}^{(i;i+1)} \,. \tag{68}$$

The numerical tests in Section 8.5, in the context of blast-type flows, show that the proposed method indeed conserves total energy within machine precision.

5   A multi-scale, residual-based hourglass control

The present section develops an analysis of the Lagrangian shock hydrodynamics equations, using an approach similar to [18, 19, 24]. The final goal is to *stabilize hourglass instabilities* while *retaining the global conservation properties* of the underlying discretization. A *minimal* approach is pursued, in the sense that the simplest and most efficient expression for the hourglass control term is sought. In the case of materials with no shear strength, the proposed strategy leads to a stabilization term in the form of a *pressure enrichment*, very easy to incorporate in state-of-the-practice hydrocodes.

5.1   Variational multi-scale analysis

Assume that the exact solution for the state $\boldsymbol{Y} = [\boldsymbol{x}^T, \boldsymbol{v}^T, \rho, \epsilon, p]^T \in \mathcal{S}$ of the system can be decomposed as $\boldsymbol{Y} = \boldsymbol{Y}^h + \boldsymbol{Y}'$. $\boldsymbol{Y}^h \in \mathcal{S}^h$ is the *mesh-* or *coarse*-scale solution, represented by the discrete approximation

space $\mathcal{S}^h$ used to characterize the solution on the computational grid. $\boldsymbol{Y}' \in \mathcal{S}'$ is the *subgrid-* or *fine-*scale solution, the component of the solution which cannot represented on the computational mesh. Obviously, $\mathcal{S} = \mathcal{S}^h \bigoplus \mathcal{S}'$.

In (27)-(36), the explicit notations $\boldsymbol{\psi}_\kappa^h$ and ψ_γ^h were used to indicate that the equations for the *exact* state of the system are tested on the discrete test function space $\mathcal{V}^h$. The superscript "h" for the components of the solution $\boldsymbol{Y}^h$ was omitted in most of the derivations in Section 4, since in that case there was no risk of confusion. In the discussion that follows, however, it is important to precisely account for the fine- and coarse-scale spaces. Hence:

$$\boldsymbol{v} = \boldsymbol{v}^h + \boldsymbol{v}' \,, \tag{69}$$

$$\rho_0 = \rho_0^h + \rho_0' \,, \tag{70}$$

$$\rho = \rho^h + \rho' \,, \tag{71}$$

$$\boldsymbol{\sigma} = \boldsymbol{\sigma}^h + \boldsymbol{\sigma}' \,, \tag{72}$$

$$\epsilon = \epsilon^h + \epsilon' \,. \tag{73}$$

$$\tag{74}$$

Using the previous decomposition, (20) and (21) reduce to

$$\int_{\Omega_0} \boldsymbol{\psi}_\kappa^h \cdot (\rho_0^h + \rho_0')(\dot{\boldsymbol{v}}^h + \dot{\boldsymbol{v}}') \, \mathrm{d}\Omega_0 + \int_\Omega (\nabla_{\boldsymbol{x}}^s \boldsymbol{\psi}_\kappa^h) : (\boldsymbol{\sigma}^h + \boldsymbol{\sigma}') \, \mathrm{d}\Omega = 0 \,, \tag{75}$$

$$\int_{\Omega_0} \psi_\gamma^h (\rho_0^h + \rho_0')(\dot{\epsilon}^h + \dot{\epsilon}') \, \mathrm{d}\Omega_0 - \int_\Omega \psi_\gamma^h \, (\nabla_{\boldsymbol{x}}^s(\boldsymbol{v}^h + \boldsymbol{v}')) : (\boldsymbol{\sigma}^h + \boldsymbol{\sigma}') \, \mathrm{d}\Omega = 0 \,, \tag{76}$$

where, in order to simplify the analysis, homogenous Dirichlet boundary conditions are imposed for the velocity. *No approximation* has been made so far, and the initial geometry of the computational grid, as well as the displacement field are assumed to be known *exactly*. At this point, it becomes useful to decompose the stress $\boldsymbol{\sigma}$ as follows:

$$\boldsymbol{\sigma} = -p\boldsymbol{I} + \mathrm{dev}\boldsymbol{\sigma} \,, \tag{77}$$

$$p = -\frac{\mathrm{tr}\boldsymbol{\sigma}}{3} = -\frac{1}{3} \sum_{k=1}^{n_d} \sigma_{kk} \,, \tag{78}$$

$$\mathrm{dev}\boldsymbol{\sigma} = \boldsymbol{\sigma} - \frac{\mathrm{tr}\boldsymbol{\sigma}}{3}\boldsymbol{I} = \boldsymbol{\sigma} + p\boldsymbol{I} \,. \tag{79}$$

An analogous decomposition holds for $\boldsymbol{\sigma}^h$ and $\boldsymbol{\sigma}'$, and the generic symmetric gradient of a vector $\boldsymbol{w}$:

$$\nabla_{\boldsymbol{x}}^s \boldsymbol{w} = (\nabla_{\boldsymbol{x}}^s \cdot \boldsymbol{w})\boldsymbol{I} + \mathrm{dev}(\nabla_{\boldsymbol{x}}^s \boldsymbol{w}) \,. \tag{80}$$

Therefore, the stress integrals in (75) and (76) can be recast in terms of the following expressions:

$$\int_\Omega (\nabla_{\boldsymbol{x}}^s \boldsymbol{\psi}_\kappa^h) : \boldsymbol{\sigma}^\bullet \, \mathrm{d}\Omega = -\int_\Omega (\nabla_{\boldsymbol{x}} \cdot \boldsymbol{\psi}_\kappa^h) : p^\bullet \, \mathrm{d}\Omega + \int_\Omega \mathrm{dev}(\nabla_{\boldsymbol{x}}^s \cdot \boldsymbol{\psi}_\kappa^h) : \mathrm{dev}\boldsymbol{\sigma}^\bullet \, \mathrm{d}\Omega \,, \tag{81}$$

$$\int_\Omega \psi_\gamma^h \, \nabla_{\boldsymbol{x}}^s(\boldsymbol{v}^\diamond) : \boldsymbol{\sigma}^\bullet \, \mathrm{d}\Omega = -\int_\Omega \psi_\gamma^h \, (\nabla_{\boldsymbol{x}} \cdot \boldsymbol{v}^\diamond) : p^\bullet \, \mathrm{d}\Omega + \int_\Omega \psi_\gamma^h \, \mathrm{dev}(\nabla_{\boldsymbol{x}}^s \boldsymbol{v}^\diamond) : \mathrm{dev}\boldsymbol{\sigma}^\bullet \, \mathrm{d}\Omega \,, \tag{82}$$

where $\boldsymbol{\sigma}^\bullet = \boldsymbol{\sigma}^h$ or $\boldsymbol{\sigma}'$, $p^\bullet = p^h$ or p', and $\boldsymbol{v}^\diamond = \boldsymbol{v}^h$ or $\boldsymbol{v}'$. Some additional assumptions are now needed to derive a simple stabilization operator.

18

Assumptions I (coarse-scale equations)

(i) Fine-scale terms are considered *small* with respect to coarse-scale terms. Therefore, products of fine-scale terms are neglected, being higher-order corrections.

(ii) Fine-scale components of the node positions and mesh geometry are considered negligible.

(iii) ρ_0' is considered negligible, since ρ_0 is a *datum* of the problem.

(iv) Time derivatives of the fine-scales are neglected. This *quasi-static* approximation is equivalent to assuming that the fine scales adjust instantaneously to complement the coarse scales. Some authors [9] have been arguing in favor of tracking in time the subgrid-scale component in the solution. However, this would involve the additional computational cost of storing and integrating in time the fine-scale component of the state variables. In the current work, this additional cost is avoided.

(v) The following integral is neglected:

$$\int_\Omega \psi_\gamma^h \, p^h \, \nabla_{\boldsymbol{x}} \cdot \boldsymbol{v}' \, \mathrm{d}\Omega = \sum_{e=1}^{n_{el}} \left(\psi_{\gamma;e}^h \, p_e^h \int_{\Omega_e} \nabla_{\boldsymbol{x}} \cdot \boldsymbol{v}' \, \mathrm{d}\Omega \right) , \tag{83}$$

where the subscript e indicates the element values of the piece-wise constant, discontinuous interpolation for ψ_γ^h and p^h. There are two important reasons to neglect this term. First of all, the typical velocity instabilities arising in the base Galerkin formulation are hourglass modes, whose divergence integrate to zero over each element. If an hourglass mode has to be counterbalanced, the corrective field $\boldsymbol{v}'$ must lie in the space of hourglass modes, and its divergence must integrate to zero over each element. Therefore, assuming that (83) is negligible or vanishes is equivalent to pose the correct constraint on the fine-scale velocity space. Another important reason not to include (83) is that its discretization would yield a non-conservative formulation. Because a number of non-linear, higher-order terms have been removed from the original equations, global conservation of total energy is not ensured *a priori*, but has to be checked and enforced *a posteriori*.

(vi) In order to obtain a conservative method, the term

$$\int_\Omega \psi_\gamma^h \, \mathrm{dev}(\nabla_{\boldsymbol{x}}^s \boldsymbol{v}') : \mathrm{dev}\boldsymbol{\sigma}^h \, \mathrm{d}\Omega \tag{84}$$

is also neglected. In the case of a fluid, this assumption is not needed, since $\mathrm{dev}\boldsymbol{\sigma}^h$ vanishes exactly.

With the previous assumptions, (75)–(76) reduce to:

$$0 = \int_{\Omega_0} \boldsymbol{\psi}_\kappa^h \cdot \rho_0^h \dot{\boldsymbol{v}}^h \, \mathrm{d}\Omega_0 - \int_\Omega (\nabla_{\boldsymbol{x}} \cdot \boldsymbol{\psi}_\kappa)^h \, p^h \, \mathrm{d}\Omega + \int_\Omega \mathrm{dev}(\nabla_{\boldsymbol{x}}^s \boldsymbol{\psi}_\kappa)^h : \mathrm{dev}\boldsymbol{\sigma}^h \, \mathrm{d}\Omega$$
$$- \int_\Omega (\nabla_{\boldsymbol{x}} \cdot \boldsymbol{\psi}_\kappa)^h \, p' \, \mathrm{d}\Omega + \int_\Omega \mathrm{dev}(\nabla_{\boldsymbol{x}}^s \boldsymbol{\psi}_\kappa)^h : \mathrm{dev}\boldsymbol{\sigma}' \, \mathrm{d}\Omega , \tag{85}$$

$$0 = \int_{\Omega_0} \psi_\gamma^h \rho_0^h \dot{\boldsymbol{\epsilon}}^h \, \mathrm{d}\Omega_0 + \int_\Omega \psi_\gamma^h \, (\nabla_{\boldsymbol{x}} \cdot \boldsymbol{v})^h \, p^h \, \mathrm{d}\Omega - \int_\Omega \psi_\gamma^h \, \mathrm{dev}(\nabla_{\boldsymbol{x}}^s \boldsymbol{v})^h : \mathrm{dev}\boldsymbol{\sigma}^h \, \mathrm{d}\Omega$$
$$+ \int_\Omega \psi_\gamma^h \, (\nabla_{\boldsymbol{x}} \cdot \boldsymbol{v})^h \, p' \, \mathrm{d}\Omega - \int_\Omega \psi_\gamma^h \, \mathrm{dev}(\nabla_{\boldsymbol{x}}^s \boldsymbol{v})^h : \mathrm{dev}\boldsymbol{\sigma}' \, \mathrm{d}\Omega . \tag{86}$$

19

Assumptions II (fine-scale representation)

(vii) The constitutive law of the material is assumed to have the form [12]

$$\dot{\boldsymbol{\sigma}} = \hat{\dot{\boldsymbol{\sigma}}}(\boldsymbol{\sigma}, \nabla_x \boldsymbol{v}) , \tag{87}$$

where the structure of $\hat{\dot{\boldsymbol{\sigma}}}$ is such that objectivity of the stress update procedure is ensured. Then, testing the variational formulation on the fine-scale space $\mathcal{V}'$, and applying a typical multi-scale approximation to the subgrid-scale Green's function operator [31, 30], the subgrid-scale stress $\boldsymbol{\sigma}$ can be expressed with the *ansatz*:

$$\boldsymbol{\sigma}' = -\tau \mathsf{Res}_\sigma^h , \tag{88}$$

$$\mathsf{Res}_\sigma^h = (\mathsf{LIN}(\mathsf{Res}_\sigma))^h , \tag{89}$$

$$\mathsf{Res}_\sigma = \dot{\boldsymbol{\sigma}} - \hat{\dot{\boldsymbol{\sigma}}}(\boldsymbol{\sigma}, \nabla_x \boldsymbol{v}) . \tag{90}$$

where LIN is a linearization operator and τ is an appropriate scaling term to be defined subsequently. As in many error estimation techniques, it is assumed that the error $\boldsymbol{\sigma}'$ is dependent on the numerical residual of constitutive equation, Res_σ^h.

The multi-scale approach pursued so far is very general, and may be exploited to derive stabilization techniques in the case of materials with very general constitutive laws, including solids. In the next section, materials with no shear strength is considered.

5.2 The case of materials with no shear strength

In the case of materials which do not possess shear strength, the terms $\mathrm{dev}\boldsymbol{\sigma}$, $\mathrm{dev}\boldsymbol{\sigma}^h$, and $\mathrm{dev}\boldsymbol{\sigma}'$ vanish exactly, and (85)–(86) simplify to

$$\int_{\Omega_0} \boldsymbol{\psi}_\kappa^h \cdot \rho_0^h \dot{\boldsymbol{v}}^h \, \mathrm{d}\Omega_0 - \int_\Omega (\nabla_x \cdot \boldsymbol{\psi}_\kappa)^h \, (p^h + p') \, \mathrm{d}\Omega = 0 , \tag{91}$$

$$\int_{\Omega_0} \psi_\gamma^h \rho_0^h \dot{\epsilon}^h \, \mathrm{d}\Omega_0 + \int_\Omega \psi_\gamma^h \, (\nabla_x \cdot \boldsymbol{v})^h \, (p^h + p') \, \mathrm{d}\Omega = 0 . \tag{92}$$

Remarks

1. The additional stabilization term is a pressure correction term.

2. The proposed approach maintains the original conservation properties of the proposed algorithm. In fact, all the conservation statements (60), (64), and (67) hold with the substitution $\tilde{\boldsymbol{\sigma}} = -(p^h + p')\boldsymbol{I}$.

It now remains to find an expression for the the subgrid-scale pressure p'. Using the assumption of smallness of the fine-scales, a Taylor expansion can be applied to the equation of state (16), namely

$$p' = p - p^h \approx \mathsf{LIN}(p - p^h) = (\partial_\rho \hat{p})^h \rho' + (\partial_\epsilon \hat{p})^h \epsilon' . \tag{93}$$

The linearization in (93) and the structure of the residuals for the mass conservation and internal energy equations can be exploited to yield

$$p' = -\tau \left((\partial_\rho \hat{p})^h \mathsf{Res}_\rho^h + (\partial_\epsilon \hat{p})^h \mathsf{Res}_\epsilon^h \right) , \tag{94}$$

20

where

$$\mathsf{Res}_\rho^h = (\mathsf{Res}_\rho)^h \ , \tag{95}$$

$$\mathsf{Res}_\rho = \dot{\rho} + \rho \ \nabla_x \cdot \boldsymbol{v} \ , \tag{96}$$

$$\mathsf{Res}_\epsilon^h = (\mathsf{Res}_\epsilon)^h \ , \tag{97}$$

$$\mathsf{Res}_\epsilon = \rho \dot{\epsilon} + p \ \nabla_x \cdot \boldsymbol{v} \ . \tag{98}$$

The residual Res_ρ is actually the mass balance, written in the current configuration, namely

$$0 = J^{-1}\dot{\rho}_0 = J^{-1}(\rho J)^{\cdot} = \dot{\rho} + \rho(J^{-1}\dot{J}) = \dot{\rho} + \rho\nabla_x \cdot \boldsymbol{v} \ , \tag{99}$$

and τ is an appropriate scaling term to be defined subsequently. As previously pointed out, it is consistent with many error estimation techniques to assume the error $\rho' = \rho - \rho^h$ in the density is a function of the mass conservation residual Res_ρ^h. Thus, the subgrid-scale pressure can be expressed as:

$$\begin{aligned}
p' &= -\tau \left(\partial_\rho \hat{p} \ \mathsf{Res}_\rho + \partial_\epsilon \hat{p} \ \mathsf{Res}_\epsilon \right)^h \\
&= -\tau \left(\partial_\rho \hat{p} \left(\dot{\rho} + \rho \ \nabla_x \cdot \boldsymbol{v} \right) + \partial_\epsilon \hat{p} \left(\dot{\epsilon} + \frac{p}{\rho} \ \nabla_x \cdot \boldsymbol{v} \right) \right)^h \\
&= -\tau \left(\dot{p} + \rho \left(\partial_\rho \hat{p} + \frac{p}{\rho^2} \partial_\epsilon \hat{p} \right) \nabla_x \cdot \boldsymbol{v} \right)^h \ .
\end{aligned} \tag{100}$$

To further simplify the previous expression, some thermodynamic identities are needed. The first and second law of thermodynamics combined yield the Gibbs identity [10],

$$\Theta d\eta = d\epsilon - p/\rho^2 d\rho \ , \tag{101}$$

with η the entropy per unit mass, and Θ the absolute temperature. Hence,

$$\frac{p}{\rho^2} = \left. \frac{\partial \epsilon}{\partial \rho} \right|_\eta \ . \tag{102}$$

It is easy then to derive

$$\begin{aligned}
p' &= -\tau \left(\dot{p} + \rho \left(\partial_\rho \hat{p} + \partial_\epsilon \hat{p} \left. \frac{\partial \epsilon}{\partial \rho} \right|_\eta \right) \nabla_x \cdot \boldsymbol{v} \right)^h \\
&= -\tau \left(\dot{p} + \rho \left. \frac{\partial p}{\partial \rho} \right|_\eta \nabla_x \cdot \boldsymbol{v} \right)^h \\
&= -\tau \left(\dot{p} + \rho c_s^2 \nabla_x \cdot \boldsymbol{v} \right)^h \\
&= -\tau \ \mathsf{Res}_p^h \ ,
\end{aligned} \tag{103}$$

where

$$\mathsf{Res}_p = \dot{p} + \rho c_s^2 \nabla_x \cdot \boldsymbol{v} \ , \tag{104}$$

and c_s is the (isentropic) speed of sound in the medium. Denoting with h_e the element characteristic length scale, the value of τ is defined as

$$\tau = c_\tau \frac{\Delta t}{2 \, CFL} = \frac{c_\tau}{2} \frac{\Delta t}{\max_{1 \le e \le n_{el}} \left(\frac{c_s \Delta t}{h_e} \right)} = \frac{c_\tau}{2} \min_{1 \le e \le n_{el}} \left(\frac{h_e}{c_s} \right) \ , \tag{105}$$

21

where $c_\tau = 7.0$ (values in the range $[5.0, 15.0]$ were found appropriate). Definition (105) is analogous to the one in [31, 30], and prevents the dramatic reduction of τ when the time step is small. The expression for the multi-scale stabilization tensor is then

$$\boldsymbol{\sigma}_{vms} = -p'\boldsymbol{I} = \tau \; \mathsf{Res}_p^h \boldsymbol{I} \; . \tag{106}$$

In the case of the proposed mid-point algorithm for time integration, (106) can be recast as:

$$\boxed{\boldsymbol{\sigma}_{vms} = \frac{\tau}{\Delta t} \left(p_{n+1}^h - p_n^h + \Delta t \left(\rho c_s^2 \right)_{n+1/2}^h \left(\nabla_{\boldsymbol{x}}^h \cdot \boldsymbol{v}^h \right)_{n+1/2} \right) \boldsymbol{I} \; .} \tag{107}$$

Remarks

1. For a general material, the final expression for $\boldsymbol{\sigma}_{vms}$ is more complicated than (106), since it involves also the deviator of the tensor $\boldsymbol{\sigma}'$. Specific expressions depend on the structure of the constitutive laws.

2. In order to have a non-vanishing multi-scale stabilization term, expression (107) *cannot* be integrated with a single-point quadrature at the centroid of quadrilateral or hexahedral elements, where the divergence of the velocity vanishes even if spurious hourglass modes are present. In fact, (107) must be evaluated with multi-point quadratures or equivalent difference formulas. The result summarized in (106)–(107) applies to a very general class of materials, since the only assumption made is the existence of the equation of state (16).

5.2.1 A rational thermodynamic interpretation

The structure of the *pressure residual* Res_p is related to the Clausius-Duhem inequality for an adiabatic process of a non-dissipative material. To prove this point, the approach of *rational thermodynamics* [1, 43, 44] is adopted. The energy balance equation can be arranged as:

$$\rho\Theta\dot{\eta} = -\nabla_{\boldsymbol{x}} \cdot \boldsymbol{q} + \rho r + \mathcal{D}_{int} \; , \tag{108}$$

where

$$\mathcal{D}_{int} \stackrel{\text{def}}{=} \rho\Theta\dot{\eta} - \rho\dot{\epsilon} - p\nabla_{\boldsymbol{x}} \cdot \boldsymbol{v} \; . \tag{109}$$

The Clausius-Duhem inequality [44] requires that $\mathcal{D}_{int} \geq 0$. Using mass conservation, $\nabla_{\boldsymbol{x}} \cdot \boldsymbol{v} = -\dot{\rho}/\rho$ and

$$\rho\mathcal{D}_{int} = p\dot{\rho} + \rho^2\Theta\dot{\eta} - \rho^2\dot{\epsilon} \geq 0 \; . \tag{110}$$

Assume there exists a *caloric equation of state* [10], that is, a function $\tilde{\epsilon}(\rho, \eta)$ (convex with respect to ρ^{-1} and η) such that $\epsilon = \tilde{\epsilon}(\rho, \eta)$. Substituting this into (110) yields

$$\rho\mathcal{D}_{int} = (p - \rho^2\partial_\rho\tilde{\epsilon})\dot{\rho} \; + \; \rho^2(\Theta - \partial_\eta\tilde{\epsilon})\dot{\eta} \; \geq 0 \; , \tag{111}$$

which is required to hold for all admissible thermodynamic processes. By the Coleman-Noll energy principle [1], this implies that

$$p = \rho^2\partial_\rho\tilde{\epsilon}(\rho, \eta) \quad \text{and} \quad \Theta = \partial_\eta\tilde{\epsilon}(\rho, \eta) \; . \tag{112}$$

Thus $\mathcal{D}_{int} = 0$, and (108) reduces to

$$\rho\Theta\dot{\eta} = -\nabla_{\boldsymbol{x}} \cdot \boldsymbol{q} + \rho r \; . \tag{113}$$

The only sources of entropy production are thermal diffusion and external heat sources. This is a well known result for *non-dissipative* materials [7, 44]: A process is *adiabatic* $(-\nabla_x \cdot \boldsymbol{q} + \rho r = 0)$ if and only if it is isentropic $(\dot{\eta} = 0)$. The previous developments imply the existence of a pressure function

$$p \stackrel{\text{def}}{=} \tilde{p}(\rho, \eta) = \rho^2 \partial_\rho \tilde{\epsilon}(\rho, \eta) \ . \tag{114}$$

Define by

$$c_s \stackrel{\text{def}}{=} \sqrt{\partial_\rho \tilde{p}(\rho, \eta)} \ , \tag{115}$$

the *isentropic* speed of sound in the material. The time derivative of the pressure function results in

$$\dot{p} = c_s^2 \dot{\rho} + \partial_\eta \tilde{p}(\rho, \eta) \, \dot{\eta} \ . \tag{116}$$

Again, using conservation of mass $\dot{\rho} = -\rho \nabla_x \cdot \boldsymbol{v}$ this may be written as

$$\dot{p} + \rho c_s^2 \nabla_x \cdot \boldsymbol{v} = \partial_\eta \tilde{p}(\rho, \eta) \, \dot{\eta} \ . \tag{117}$$

Assuming an adiabatic process this reduces to

$$\dot{p} + \rho c_s^2 \nabla_x \cdot \boldsymbol{v} = \mathsf{Res}_p = 0 \ , \tag{118}$$

the pressure residual.

Remark

1. In practice Res_p^h is a measure of the *entropy production* due to the numerical discretization. In regions of smooth flow, Res_p^h should vanish, but because of numerical instabilities, *numerical entropy* can be generated.

2. The previous analysis for perfect materials also shows that the assumption of smallness of the fine scales implies the concept of isentropic flow.

3. When shock waves are present in the material, the analysis in the present section does not apply. From a physical point of view, a shock wave is an infinitely thin layer in which the flow does not behave as a perfect material, due to internal dissipation mechanisms. From a numerical point of view, a shock-capturing operator typically smears the discontinuity over a few cells of the computational grid. Shock-capturing operators usually have the form of an artificial dissipation, and introduce in the material an irreversible internal mechanism.

5.2.2   Multi-scale stabilization revisited as hourglass control

To understand that the proposed pressure enrichment acts as an hourglass control, let us decompose the divergence of a vector $\boldsymbol{w}^h$ into its average value over an element and the fluctuation with respect to the average. Namely,

$$\nabla_x^h \cdot \boldsymbol{w}^h = \overline{\nabla_x^h \cdot \boldsymbol{w}^h} + \widetilde{\nabla_x^h \cdot \boldsymbol{w}^h} \ , \tag{119}$$

$$\overline{\nabla_x^h \cdot \boldsymbol{w}^h} = \frac{1}{\text{meas}(\Omega_e)} \int_{\Omega_e} \nabla_x^h \cdot \boldsymbol{w}^h \, \mathrm{d}\Omega = \frac{1}{\text{meas}(\Omega_e)} \int_{\Gamma_e} \boldsymbol{w}^h \cdot \boldsymbol{n} \, \mathrm{d}\Gamma \ . \tag{120}$$

By definition, $\overline{\nabla_x^h \cdot w^h}$ and $\widetilde{\nabla_x^h \cdot w^h}$ are orthogonal in the L^2 sense. Consider the structure of the stabilization term developed in the previous section. The expressions (91) and (92) can be rearranged as:

$$\int_{\Omega_e} (\nabla_x^h \cdot \psi_\kappa^h)\, p'\, \mathrm{d}\Omega = - \int_{\Omega_e} (\nabla_x^h \cdot \psi_\kappa^h)\tau \left(\dot{p}^h + (\rho c_s^2)^h \nabla_x^h \cdot v^h\right)\, \mathrm{d}\Omega$$

$$= - \int_{\Omega_e} (\nabla_x^h \cdot \psi_\kappa^h)\tau \left(\dot{p}^h + (\rho c_s^2)^h \overline{\nabla_x^h \cdot v^h} + \widetilde{\nabla_x^h \cdot v^h}\right)\, \mathrm{d}\Omega$$

$$= - \int_{\Omega_e} (\nabla_x^h \cdot \psi_\kappa^h)\tau \left(\dot{p}^h + (\rho c_s^2)^h \overline{\nabla_x^h \cdot v^h}\right)\, \mathrm{d}\Omega$$

$$- \tau \left(\rho c_s^2\right)^h \int_{\Omega_e} \left(\nabla_x^h \cdot \psi_\kappa^h\right)\left(\widetilde{\nabla_x^h \cdot v^h}\right)\, \mathrm{d}\Omega$$

$$= -\tau \left(\dot{p}^h + \rho c_s^2\, \overline{\nabla_x^h \cdot v^h}\right)_e \int_{\Omega_e} \left(\nabla_x^h \cdot \psi_\kappa^h\right)\, \mathrm{d}\Omega + \mathsf{HG}_{1;e}\,, \tag{121}$$

$$\int_{\Omega_e} (\nabla_x^h \cdot v^h)\, p'\, \mathrm{d}\Omega = -\tau \left(\dot{p}^h + (\rho c_s^2)^h\, \overline{\nabla_x^h \cdot v^h}\right)_e \overline{\nabla_x^h \cdot v^h}\, \mathrm{meas}(\Omega_e) + \mathsf{HG}_{2;e}\,, \tag{122}$$

with

$$\mathsf{HG}_{1;e} = -\tau \int_{\Omega_e} \left(\rho c_s^2\right)^h \left(\widetilde{\nabla_x^h \cdot \psi_\kappa^h}\right)\left(\widetilde{\nabla_x^h \cdot v^h}\right)\, \mathrm{d}\Omega\,, \tag{123}$$

$$\mathsf{HG}_{2;e} = -\tau \int_{\Omega_e} \left(\rho c_s^2\right)^h \left(\widetilde{\nabla_x^h \cdot v^h}\right)^2\, \mathrm{d}\Omega\,. \tag{124}$$

To provide an interpretation of (121)–(122), it is important to realize that, for the proposed second-order in time algorithm,

$$\left(\dot{p}^h + (\rho c_s^2)^h\, \overline{\nabla_x^h \cdot v^h}\right)_e = \left(\dot{p}^h - (c_s^2)^h\, \dot{\rho}^h\right)_e$$

$$\approx \Delta t \left(p_{n+1}^h - p_n^h - (c_s^2)_{n+1/2}^h \left(\rho_{n+1}^h - \rho_n^h\right)\right)_e$$

$$= O(\Delta t^2)\,. \tag{125}$$

When hourglass modes arise, the expression in (125) tends to be much smaller than the terms $\mathsf{HG}_{1;e}$ and $\mathsf{HG}_{2;e}$, which represent the discretization of a $(\nabla_x \cdot)$-$(\nabla_x \cdot)$ dissipative operator acting on the hourglass modes.

Remarks

1. In regions where a shock is present and the artificial viscosity operator is active, (125) may not hold.

2. Notice that $\mathsf{HG}_{1;e}$ and $\mathsf{HG}_{2;e}$ scale with the square of the speed of sound and the density of the material, similarly to many hourglass control viscosities [4].

3. In order for the hourglass control to work, the $\mathsf{HG}_{1;e}$ and $\mathsf{HG}_{2;e}$ terms must be evaluated at locations where the discrete divergence operator is non-vanishing. Therefore, full integration (or equivalent difference formulas) are required. However, the integration involves only kinematic terms, and not the thermodynamic variables, which need only one evaluation per element.

The previous observations can also be used to define an alternative class of hourglass operators. The basic idea is to define a time interpolation for $(\rho c_s^2)^h$, so that, element-by-element, $(\dot{p}^h + \rho^h c_s^2\, \overline{\nabla_x^h \cdot v^h})_e$

vanishes exactly. This can be done with a *secant approximation* of ρc_s^2, enforcing explicitly

$$\left(\rho c_s^2\right)_{n+1/2}^h \overset{\text{def}}{=} \frac{p_{n+1}^h - p_n^h}{\Delta t \overline{\nabla_{\boldsymbol{x}}^h \cdot \boldsymbol{v}^h}} . \tag{126}$$

If this is the case, the stabilization term reduces to:

$$\int_{\Omega_e} \left(\nabla_{\boldsymbol{x}}^h \cdot \boldsymbol{\psi}_\kappa^h\right) p' \, \mathrm{d}\Omega = \mathsf{HG}_{1;e} , \tag{127}$$

$$\int_{\Omega_e} \left(\nabla_{\boldsymbol{x}}^h \cdot \boldsymbol{v}^h\right) p' \, \mathrm{d}\Omega = \mathsf{HG}_{2;e} . \tag{128}$$

This alternative class of stabilization operators is clearly augmenting the original variational formulation by means of a *purely* dissipative operator. A different choice of the scaling for τ is also possible in this case, namely,

$$\tilde{\tau}_e = \tilde{\tau}|_{\Omega_e} = \tau \frac{h_e}{c_s \, \Delta t} , \tag{129}$$

where this time $c_\tau = 3.0$ (values in the range $[1.0, 7.0]$ were found appropriate), and h_e is a characteristic mesh length, for which many possible definitions can be used. One of them is $h_e \, (\text{meas}(\Omega_e))^{1/n_d}$. If this is the case, then the stabilization term introduced would scale like the viscous part of the Flanagan-Belytschko hourglass control [11, 45, 12, 4].

5.2.3 Multi-scale stabilization in three dimensions

By design, the proposed hourglass control detects only those unstable modes whose divergence is non-zero. This is not unexpected, since the residual stabilization is tied to the physics of the system to be simulated. Specifically, any material satisfying a constitutive law like (15) does not possess shear strength, but can only react to changes in volume (or, equivalently, a non-zero velocity divergence). This poses interesting implications. In two dimensions, none of the hourglass modes are divergence-free, and the stabilization mechanisms are straightforward to understand. In three dimensions, however, the situation is different. In fact, for a hexahedral element, the space $\mathcal{H}$ of the modes of hourglass deformations is spanned by 12 hourglass eigenmodes [29]. The space $\mathcal{H}$ can be further divided into two subspaces (see Fig. 2):

1. The space $\mathcal{H}_{div}$ of modes which are divergence-free *only* at the centroid of the element, but are not divergence-free elsewhere in the element. Specifically,

$$\mathcal{H}_{div} = \text{span} \left\{ \begin{Bmatrix} \xi_1 \xi_2 \xi_3 \\ 0 \\ 0 \end{Bmatrix}, \begin{Bmatrix} 0 \\ \xi_1 \xi_2 \xi_3 \\ 0 \end{Bmatrix}, \begin{Bmatrix} 0 \\ 0 \\ \xi_1 \xi_2 \xi_3 \end{Bmatrix}, \begin{Bmatrix} \xi_1 \xi_2 \\ 0 \\ 0 \end{Bmatrix}, \begin{Bmatrix} 0 \\ \xi_2 \xi_3 \\ 0 \end{Bmatrix}, \begin{Bmatrix} 0 \\ 0 \\ \xi_3 \xi_1 \end{Bmatrix} \right\} , \tag{130}$$

where ξ_i is the ith coordinate in the parent domain. These modes are dissipated by the multi-scale hourglass control.

2. The set $\mathcal{H}_{shear}$ of *point-wise divergence-free* modes, associated with *purely deviatoric* motion. Namely,

$$\mathcal{H}_{shear} = \text{span} \left\{ \begin{Bmatrix} \xi_2 \xi_3 \\ 0 \\ 0 \end{Bmatrix}, \begin{Bmatrix} 0 \\ \xi_1 \xi_3 \\ 0 \end{Bmatrix}, \begin{Bmatrix} 0 \\ 0 \\ \xi_1 \xi_2 \end{Bmatrix}, \begin{Bmatrix} \xi_3 \xi_1 \\ -\xi_3 \xi_2 \\ 0 \end{Bmatrix}, \begin{Bmatrix} 0 \\ \xi_1 \xi_2 \\ -\xi_1 \xi_3 \end{Bmatrix}, \begin{Bmatrix} -\xi_2 \xi_1 \\ 0 \\ \xi_2 \xi_3 \end{Bmatrix} \right\} . \tag{131}$$
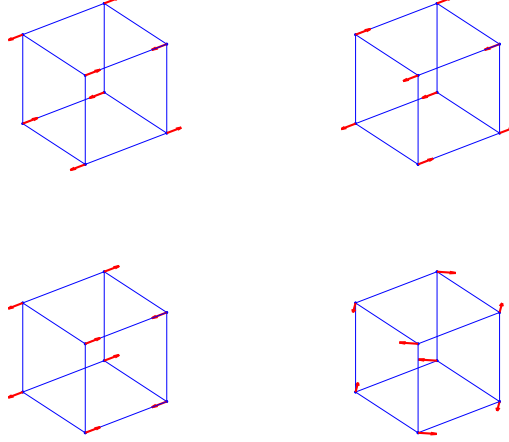
Figure 2. Sketch of the typical hourglass modes in three dimensions. The two modes on the left column are associated with the space $\mathcal{H}_{div}$, and their divergence is zero only at the centroid of the element. The two modes on the right column are associated with the space $\mathcal{H}_{shear}$ of divergence-free shear modes. The four hourglass modes shown are associated with the ξ_1 coordinate in the parent domain. The other eight modes are obtained by rotation, and they are aligned along the ξ_2 and ξ_3 axes, respectively.

Given the structure of (103), it is clear that these modes are not dissipated by the multi-scale stabilization. On the contrary, for a solid, the constitutive law yields a Cauchy stress which is more complex than a simple pressure. As a consequence, the fine scale stress also possesses a deviatoric component, which provides stabilization for the modes in $\mathcal{H}_{shear}$.

It becomes clear at this point what was referred in the Introduction as the Q1/P0-element dilemma in fluids: On the one hand, modes in $\mathcal{H}_{shear}$ require control; on the other hand, any shear damping would be unphysical, and may destroy important features of the flow.

The multi-scale approach highlights this paradox with great precision, since physical stabilization is only provided to the modes in $\mathcal{H}_{div}$. An important discussion on some implications in the case of unstable shear modes and SUPG stabilization is provided in the next two remarks.

Remarks

1. It can also be shown that SUPG stabilized methods for piecewise-linear, continuous discretizations do not damp divegence-free hourglass modes in $\mathcal{H}_{shear}$. As a simple example, consider a frictionless, Euler flow problem on a Cartesian mesh in which the velocity vector $\boldsymbol{v}$ is seeded with a point-wise divergence-free mode in $\mathcal{H}_{shear}$. It is unimportant whether the mesh is fixed (Eulerian) or tied to the material (Lagrangian). For the sake of simplicity, all thermodynamic variables are assumed initially constant. SUPG operators are introduced to stabilize numerical computations by means of a combination of the residuals Res_ρ^h, Res_ϵ^h, and $\mathbf{Res}_v^h$, where

$$\mathbf{Res}_v = \rho \dot{\boldsymbol{v}} + \nabla_{\boldsymbol{x}} p \; . \tag{132}$$

Since the pressure is constant, and the velocity mode is divergence-free, it is easy to realize that $\dot{\rho} = \dot{\epsilon} = \dot{p} = 0$ and $\dot{\boldsymbol{v}} = \boldsymbol{0}$. As a result, $\mathsf{Res}_\rho^h = \mathsf{Res}_\epsilon^h = 0$, and $\mathbf{Res}_v^h = \boldsymbol{0}$. Therefore, the entire SUPG operator vanishes, and any velocity field in $\mathcal{H}_{shear}$ is undamped. This is a manifestation of the residual approach: The constitutive law of the material is unable to produce shear forces. Notice, however, that no instabilities related to modes in $\mathcal{H}_{shear}$ are mentioned in the vast literature of SUPG methods for the compressible Euler equations [25, 22, 21, 20, 14, 15, 16, 27, 33, 37, 36, 41, 42, 38, 39, 40]. This seems to indicate that the underlying finite element space is playing a crucial role in preventing shear modes, an aspect which may be the object of future investigation.

2. The previous remark can also be considered from a reverse perspective. In very complex flows, such as the ones generated by multiple interactions of curved shocks, modes in $\mathcal{H}_{shear}$ may be generated as physical features.

In order to develop a stable formulation in three dimensions, an additional hourglass-control operator is added, in the form of an artificial stress:

$$\boldsymbol{\sigma}_{hg} = \nu_{hg} \, \widetilde{\mathrm{dev}\nabla_x^s\boldsymbol{v}} \,, \tag{133}$$

$$\nu_{hg} = \left(c_{hg;1} \, h_e^2 \, \|\widetilde{\mathrm{dev}\nabla_x^s\boldsymbol{v}}\|_{l^2} \;+\; c_{hg;2} \, h_e \, c_s \right) e^{c_{hg;3} \frac{V_{e;n+1}}{V_{e;n}}} \,, \tag{134}$$

$$\widetilde{\mathrm{dev}\nabla_x^s\boldsymbol{\psi}}_\kappa = \mathrm{dev}\nabla_x^s\boldsymbol{w} - \overline{\mathrm{dev}\nabla_x^s\boldsymbol{w}} \,, \tag{135}$$

where $\|\boldsymbol{T}\|_{l^2}$ represent the Frobenius norm of the tensor $\boldsymbol{T}$, that is $\|\boldsymbol{T}\|_{l^2}^2 = \boldsymbol{T} : \boldsymbol{T}$, and $V_{e;\bullet}$ is the element volume at time $t_\bullet$. The constants are chosen to be $c_{hg;1} = 3.0$, $c_{hg;2} = 0.06$, and $c_{hg;3} = 2.0$.

Remarks

1. The form of (133) is such that the fluctuation of the deviator of the symmetric gradient of the velocity field is damped. In terms of kinematics, $\widetilde{\mathrm{dev}\nabla_x^s\boldsymbol{v}}$ is associated with the modes in $\mathcal{H}_{shear}$, which are therefore the target of the proposed damping operator.

2. The proposed approach does not affect the *consistency* of the method, and, consequently, the convergence rates, since it applies to gradient fluctuations.

3. The constant $c_{hg;1}$ is considerably larger than the constant $c_{hg;2}$, implying that the acoustic scaling is considered of minor importance. This is an acceptable choice since the tensor $\boldsymbol{\sigma}_{hg}$ does not carry any physical meaning.

4. The exponential (non-dimensional) term

$$e^{c_{hg;3} \frac{V_{e;n+1}}{V_{e;n}}} \tag{136}$$

increases the viscosity in expansion regions, where the hourglass modes are more likely to grow, and reduces it in compression regions, where the modes are more likely to reduce their intensity. The latter is a very important feature in implosion computations, since an overly strong hourglass viscosity may result in computational failure, as documented in the numerical computations of Section 8. Usually values in the range $[1.0, 3.0]$ were found appropriate, for the constant $c_{hg;3}$.

5. There is a substantial amount of freedom in the design of the hourglass viscosity operator and this is a direct consequence of the multi-scale perspective. One can take advantage of this fact to develop a more flexible approach to hourglass stabilization.

6. Finally, it is important to realize that the multi-scale operator and the hourglass viscosity may be active at the same time on some of the elements of the discretization. Since the hourglass operator is a second-order correction, and acts on divergence-free fluctuations of the velocity field, it is reasonable to assume it does not produce a large perturbation to the Clausius-Duhem residual (104).

7. In the case of a solid, the proposed hourglass viscosity would be unnecessary, since the residual of the stress update equation can provide shear-stabilization terms. This is due to the fact that contrary to a fluid, a typical solid *does* possess shear strength.

6 Artificial viscosity and discontinuity capturing operator

The discontinuity capturing operator is implemented as follows:

$$\boldsymbol{\sigma}_{art} = \begin{cases} \rho \, \nu_{art} \nabla_{\boldsymbol{x}}^{s} \, \boldsymbol{v} \,, & \text{if } \nabla_{\boldsymbol{x}} \cdot \boldsymbol{v} < 0 \,, \\ \boldsymbol{0}_{n_d \times n_d} \,, & \text{otherwise} \,. \end{cases} \tag{137}$$

Remarks

1. The use of the symmetric gradient in the definition of $\boldsymbol{\sigma}_{art}$ ensures, at the continuum level, objectivity of the artificial viscosity operator.

2. The definition (137) is more effective in damping artificial pure shear motion, with respect to the more common definition [5]

$$\boldsymbol{\sigma}_{art} = - \left(\rho \, \nu_{art} \nabla_x \cdot \boldsymbol{v} \right) \boldsymbol{I} \,. \tag{138}$$

Artificially produced homogeneous shear motion can have disruptive consequences on shock hydrodynamics computations of fluids, since it is not resisted by hourglass controls (of any type), nor the discretized physical stress.

Several choices of the artificial viscosity parameter ν_{art} are possible. Among the most commonly used,

$$\nu_{Kur} = \left(c_{Kur_2} \frac{\gamma - 1}{4} |\nabla_{\boldsymbol{x}} \cdot \boldsymbol{v}| h_{art} + \sqrt{\left(c_{Kur_2} \frac{\gamma - 1}{4} |\nabla_{\boldsymbol{x}} \cdot \boldsymbol{v}| h_{art} \right)^2 + c_{Kur_1}^2 c_s^2} \right) h_{art} \,, \tag{139}$$

$$\nu_{dyna} = c_1 c_s h_{art} + c_2 |\nabla_{\boldsymbol{x}} \cdot \boldsymbol{v}| h_{art}^2 \,, \tag{140}$$

where, the values $c_1 = 1.2$ and $c_2 = 0.5$ have been used in the computations of Section 8. Also, $c_{Kur_1} = c_{Kur_2} = 1$, and γ is the isentropic constant in the gas. The expression for the so-called Kuropatenko viscosity ν_{Kur} [26] holds only for an ideal gas, while ν_{dyna} is general enough to include all materials satisfying (15)–(16). The length-scale h_{art} needs to be defined according to one main requirement: It should *stably* sample a mesh length along the normal to the shock front. This means that, for a given mesh, h_{art} should not vary abruptly for small changes in the direction of the shock normal. An effective definition was found to be

$$h_{art} = \frac{2}{\sqrt{\boldsymbol{n}_{sh}^T \left(\boldsymbol{F}_\square \boldsymbol{F}_\square^T \right)^{-1} \boldsymbol{n}_{sh}}} \,, \tag{141}$$

$$\boldsymbol{F}_\square = \frac{\partial \boldsymbol{x}}{\partial \boldsymbol{\xi}} \,, \tag{142}$$
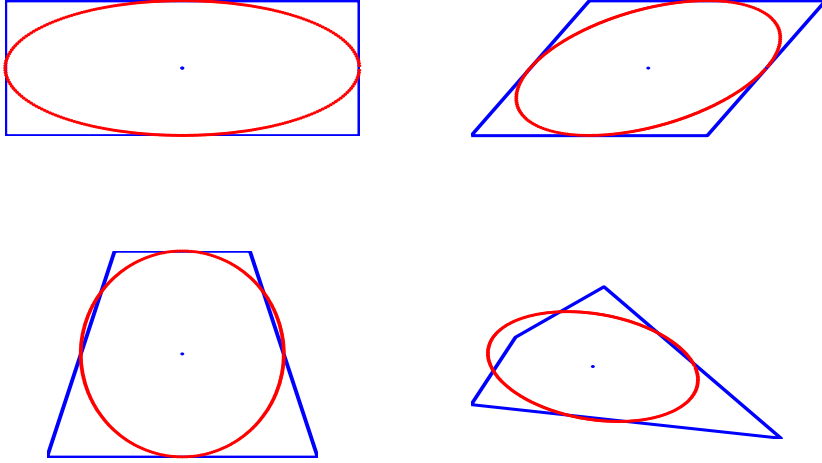
Figure 3. Sketch of the length-scale h_{art} as a function of the direction of $\boldsymbol{n}_{sh}$. The plots show the envelope of h_{art} as the angle that $\boldsymbol{n}_{sh}$ forms with the x_1-axis varies from 0 to 360 degrees. Notice the smooth transition of the length-scale near the corners of the elements.

where $\boldsymbol{n}_{sh}$ is a unit vector in the direction normal to the shock front, and $\boldsymbol{F}_{\square}$ the gradient of the mapping from the parent domain to the element in the current configuration. In practice, $\left(\boldsymbol{F}_{\square}\boldsymbol{F}_{\square}^{T}\right)$ measures the *stretch* in the direction given by $\boldsymbol{n}_{sh}$. A plot of the envelope of h_{art} as the shock normal angle spans the interval $[0, 360]$-degrees is presented in Figure 3, for various quadrilateral elements. This definition is analogous to the one adopted in [23]. An effective approximation to $\boldsymbol{n}_{sh}$ is given by:

$$\boldsymbol{n}_{sh} = \frac{\nabla_{\boldsymbol{x}} f_{\boldsymbol{b}}}{||\nabla_{\boldsymbol{x}} f_{\boldsymbol{b}}||} \ , \tag{143}$$

$$f_{\boldsymbol{b}} = \frac{||\boldsymbol{v}||_{l^2}}{\max_{1 \le e \le n_{el}}(||\boldsymbol{v}||_{l^2})} + 10^{-3}\frac{\hat{\rho}}{\max_{1 \le e \le n_{el}}(\hat{\rho})} \ , \tag{144}$$

where $||\boldsymbol{v}||_{l^2} = \sqrt{\boldsymbol{v} \cdot \boldsymbol{v}}$ is the velocity magnitude, and $\hat{\rho}$ is the nodal projection of the density, namely

$$\hat{\rho} = \sum_{A=1}^{n_{np}} \hat{\rho}_A N_A(\boldsymbol{X}) \ , \tag{145}$$

$$\hat{\rho}_A = \frac{\overset{n_{el}}{\underset{e=1}{\mathbf{A}}} \int_{\Omega_e} N_A \ \rho \ \mathrm{d}\Omega}{\overset{n_{el}}{\underset{e=1}{\mathbf{A}}} \int_{\Omega_e} N_A \ \mathrm{d}\Omega} = \frac{\overset{n_{el}}{\underset{e=1}{\mathbf{A}}} \left(\rho_e \int_{\Omega_e} N_A \ \mathrm{d}\Omega\right)}{\overset{n_{el}}{\underset{e=1}{\mathbf{A}}} \int_{\Omega_e} N_A \ \mathrm{d}\Omega} \ , \tag{146}$$

with $\mathbf{A}$ the assembly operator [17, 4].

Remarks

1. The definitions (143)–(144) are meant to use primarily the gradient of the velocity magnitude as a measure of the shock normal. There are a number of cases – such as implosions with radial or

29

spherical symmetry – in which the simple use of the gradient of the velocity norm may result too noisy in the region preceding the shock location. This is why f_b rather then $||\boldsymbol{v}||_{l^2}$ is introduced. The use of the gradient of the projected nodal density is reminiscent of [42].

2. The tensor $\boldsymbol{\sigma}_{art}$ just defined is evaluated at the midpoint in time, together with the other terms contributing to the nodal forces. Collocation at the mid-point in time ensures *incremental objectivity* of the tensor $\boldsymbol{\sigma}_{art}$ [34].

7 General considerations on implementation

7.1 Numerical quadratures

First and foremost, as already noted, the divergence of the velocity in the pressure residual Res_p^h vanishes at the centroid of quadrilateral or hexahedral elements. Therefore, four/eight-point quadratures must be used to compute the stabilization term. Notice that all other terms in the pressure residual are constant over each of the elements, and do not need multi-point evaluation. The hourglass control for divergence-free shear modes in three dimensions also require multi-point quadratures.

Second, when the shock capturing operator is active, non-linear coupling effects may take place between the artificial viscosity and the multi-scale stabilization operator, as already mentioned. The optimal choice is to integrate *both* the artificial viscosity and the multi-scale operator with the same quadrature rule. With this approach, incidentally, the computational cost for the multi-scale operator is negligible with respect to the cost of the artificial viscosity, since the divergence of the velocity is needed by both. Some examples of the effects of single-point and multi-point integration for the viscosity are presented in Section 8.3.

To understand why superior results are obtained when the multi-scale and artificial viscosity operators share the same quadrature rule, one needs to recall that where the artificial dissipation is active, the multi-scale approach is not strictly applicable. A single-point evaluation of the artificial viscosity is equivalent to enforcing that the value of the artificial viscosity is constant over the entire element. Especially in the case of rapid transients, this may be a very coarse approximation. Indeed, on a particular element of the mesh, the artificial viscosity may be active only in just a few of the quadrature points. Single-point integration redistributes the effect of the artificial viscosity over the entire element, generating a spurious pressure residual at the quadrature points where there should be no artificial dissipation. In the end, the multi-scale approach, which leverages a local evaluation of the residual, may be affected by the incorrect evaluation of the artificial dissipation.

In terms of quadrature rules, the details of the implementation can be then summarized as follows:

1. The integral of the physical stress term $\boldsymbol{\sigma}$ is evaluated with a single-point quadrate at the centroid of the element.

2. The multi-scale residual-based stabilization operator is computed with multi-point quadratures.

3. Unless otherwise specified, it should be implicitly assumed that the artificial viscosity operator is integrated with full quadrature.

7.2 Hourglass stabilization and artificial viscosity parameters

Most of the numerical results are obtained using the multi-scale operator as defined in (107). This method is denoted by VMS-I, and the choice $c_\tau = 7$ is made to evaluate expression (105) (a range of recommended values could be $[5.0, 15.0]$). In addition, some computations using the approach of (123)–(124) are performed. This method is denoted by VMS-II, and the the choice $c_\tau = 3$ is made to evaluate expression (129) (a range of recommended values could be $[1.0, 5.0]$). In three dimensions, VMS-I and VMS-II are complemented with the deviatoric fine-scale artificial viscosity detailed in (133)–(135).

In order to compare the proposed multi-scale approach with existing approaches, a viscous-type hourglass control *à la* Flanagan-Belytschko [4, 11, 12, 45] is also used: This method is referred to as FB. Unless otherwise specified, the constant parameter is chosen to be $c_{FB} = 0.15$. Typical recommended values [12] span the interval $[0.05, 0.15]$. The choice of making the hourglass control as dissipative as possible within the recommended range has the purpose of maximizing robustness.

An artificial viscosity of type (140) is used in all computations, with $c_1 = 0.5$ and $c_2 = 1.2$.

7.3 CFL condition

The following constraint on the time step has been adopted:

$$\Delta t \;=\; CFL \, \frac{h_{min}^2}{\nu_{tot} + \sqrt{\nu_{tot}^2 + (c_s h_{min})^2}} \;, \tag{147}$$

$$\nu_{tot} \;=\; \nu_{art} + \max(c_s h_e, \nu_{hg}) \;, \tag{148}$$

$$\nu_{hg} \;=\; \begin{cases} \tau \Delta t c_s^2 \,, & \text{for VMS-I} \,, \\ \tilde{\tau} \Delta t c_s^2 \,, & \text{for VMS-II} \,, \\ c_{FB} h_e c_s \,, & \text{for FB} \,, \end{cases} \tag{149}$$

$$h_{min} \;=\; \min_{1 \le A \le n_{np}} h_A \;. \tag{150}$$

Here, h_{min} is the minimum of the node distances. This definition of the time-step constraint is similar to the one adopted in the LS-DYNA algorithm [13].

8 Numerical computations

8.1 Acoustic pulse computations and hourglass control

A very interesting test to check the the effect of the hourglass control is to propagate an acoustic pulse on a mesh in which the nodes are initially located according to an hourglass pattern (see Fig. 4(a)). For this
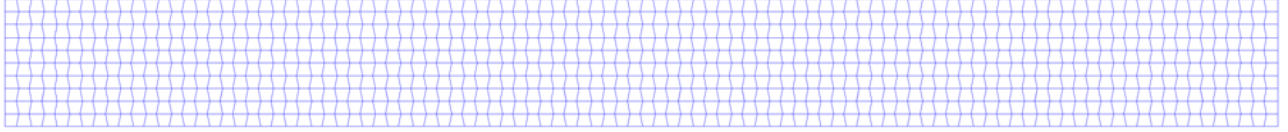
(a) Initial mesh with nodes positioned according to a typical hourglass pattern.
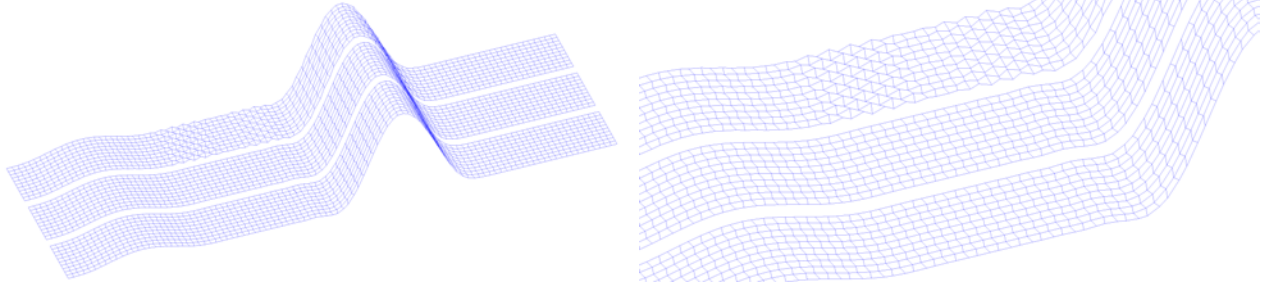
(b) Elevation plot of the x_1-component of the velocity. Top: No hourglass control. Center: VMS-I. Bottom: FB.

(c) Zoomed view from Figure 4(b). Top: No hourglass control. Center: VMS-I. Bottom: FB.

Figure 4. Acoustic pulse test on an hourglass-shaped mesh. Notice the fluctuations in the velocity at the foot of the left- and right-moving acoustic waves, in the case of no hourglass control (Fig. 4(c)). These instabilities are absent when the VMS-I or FB stabilization is applied.

specific test, the shock-capturing operator is not applied. The initial conditions are

$$v_0 = \omega \,, \tag{151}$$
$$\rho_0 = 1 + \omega \,, \tag{152}$$
$$p_0 = 1 + \omega \,, \tag{153}$$
$$\omega(X) = \begin{cases} 0.1(1 - \cos((2\pi/\lambda)(X - X_{off})) \,, & 0 \le X - X_{off} \le \lambda \,, \\ 0 \,, & \text{otherwise} \,, \end{cases} \tag{154}$$

where λ, the wavelength is taken equal to one fourth of the length the domain Ω_0, and $X_{off} = -\lambda$. As time progresses three waves are generated (see Fig. 4(b)):

1. A large amplitude acoustic wave moving from left to right.

2. A smaller amplitude acoustic wave moving from right to left.

3. A standing (i.e., motionless) entropy wave, characterized by a fluctuation in density and internal energy (not visible in Fig. 4(b)).

It can be seen in Figure 4(c) that, when no control is applied, the hourglass modes manifest themselves as oscillations in the velocity. Since the pressure is approximated by piece-wise functions which are constant over each element, it is well-known that hourglass modes would arise even if multiple-point quadrature were used. This fact was confirmed in computations, not reported here for the sake of brevity. As the VMS-I stabilization is applied, the instabilities disappear. For the purposed of comparison, Figure 4(c) also shows the results for the FB hourglass control. The results of the VMS-I and FB stabilizations are virtually identical.

32
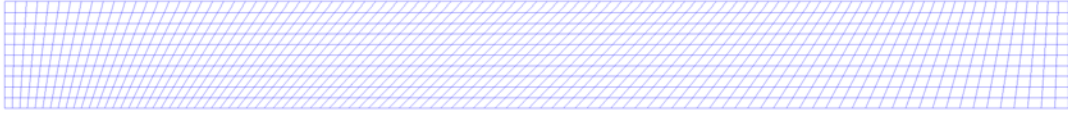
(a) Initial mesh.
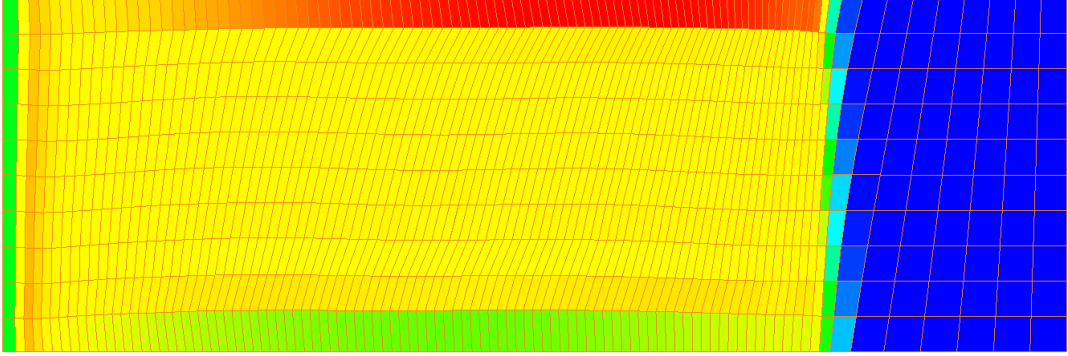
(b) Density color plot at $T = 0.7$: VMS-I stabilization.
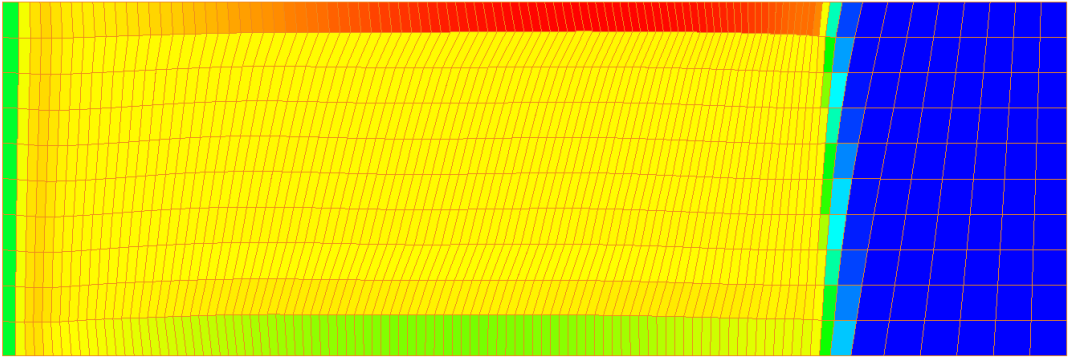
(c) Density color plot at $T = 0.7$: FB stabilization.

Figure 5. Saltzmann test: Comparison between VMS-I and FB.

8.2 Saltzmann test

The Saltzmann test evaluates the ability of a distorted mesh to capture the features of a planar shock. A rectangular domain of gas ($\gamma = 5/3$) is initially at rest. The left boundary moves with unit velocity and generates a compression shock propagating from left to right through the domain. All other boundary conditions are of "roller" type, that is, zero normal velocity (and, consequently, zero normal displacement). The Saltzmann test is both a robustness and an accuracy test. The initial mesh, an integral part of the test case, is presented in Figure 5(a). Computations are performed at $CFL = 0.8$.

As it can be seen from the results in Figures 5(b), 5(c), and 6), aside from some over-/under-shoot near the boundaries, the numerical and exact solution show fair agreement. A reason for the over-/under-shoot near the boundaries may be the inaccurate representation of homogeneous gradients on general unstructured meshes for the piece-wise constant approximation of the pressure [8]. An analogous result
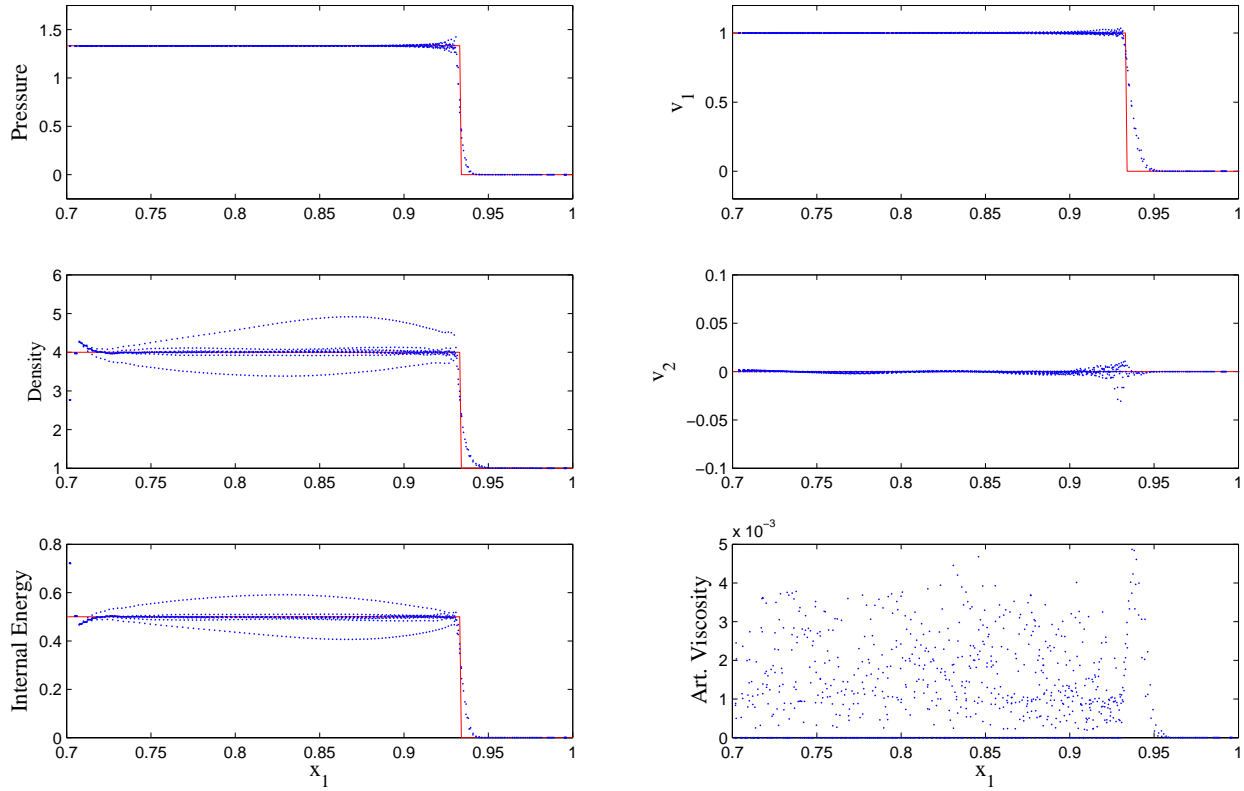
Figure 6. Saltzmann test: The VMS-I approach is compared against the exact solution. The solution is plotted as a function of the coordinate x_1. On the left column: Pressure, density and internal energy. On the right column: Horizontal velocity v_1, vertical velocity v_2, and artificial viscosity ν_{art}. The exact solution is represented by the continuous line, the dots represent *all* the nodal values of the numerical solution (the x_2-coordinate locations are projected onto a single plane).

is obtained when the Flanagan-Belytschko hourglass control is applied instead of the multi-scale control (Fig. 5(c)).

8.3   Sedov test in two dimensions

The Sedov test is a multi-dimensional blast test. An exact solution, which possesses cylindrical symmetry, is derived with self-similarity arguments in [32].

8.3.1   Sedov test on a Cartesian quadrant

The proposed version of the Sedov blast test is performed on the $[0, 1.1] \times [0, 1.1]$ quadrant, subdivided into 45×45 squares, and assesses the ability of the method to respect the cylindrical symmetry. The

(a) Mesh deformation, no stabilization.

(b) Mesh deformation, VMS-I.

(c) Density color plot, no stabilization.

(d) Density color plot, VMS-I.
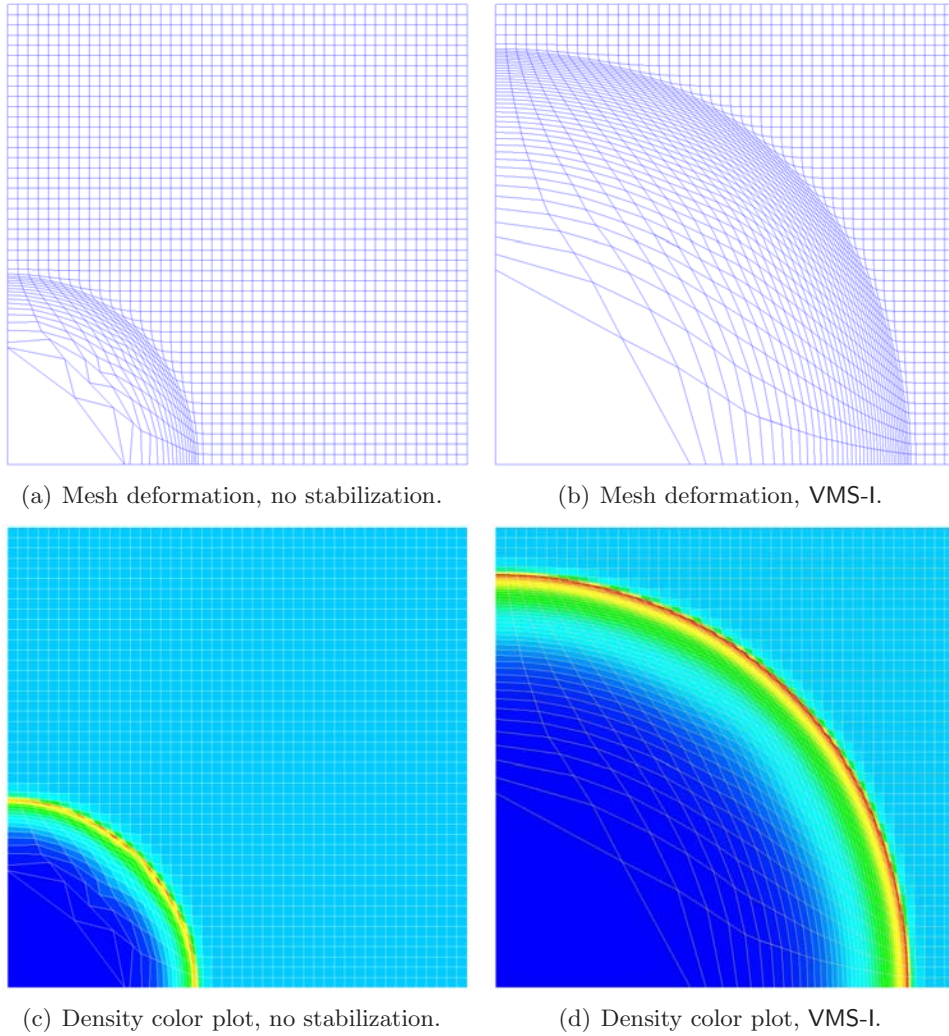
Figure 7. Two-dimensional Sedov test. Left Column: No hourglass stabilization. Right column: VMS-I with full-integration of the shock-capturing term. When no stabilization is applied, it is clearly visible a pronounced hourglass pattern, which forces the computation to stop before completion.

initial mesh configuration, for the sake of brevity, is not shown. The initial density has a uniform unit distribution, $\gamma = 1.4$, and the energy is "zero" (actually, 10^{-14}) everywhere, except the first square zone on the bottom left corner of the quadrant, near the origin, where it takes the value 409.7. Figure 7 shows a comparison of the results when no stabilization and VMS-I stabilization are applied. When no stabilization is applied, the computation cannot be run to completion, since an hourglass pattern forms in the mesh (see Fig. 7(a)). As a consequence, the distance between some of the nodes decreases progressively during the simulation, forcing the same behavior in the time step, due to the CFL constraint. On the contrary, the VMS-I approach runs to completion and with a very smooth mesh and density profiles (Figs. 7(b) and 7(d)).
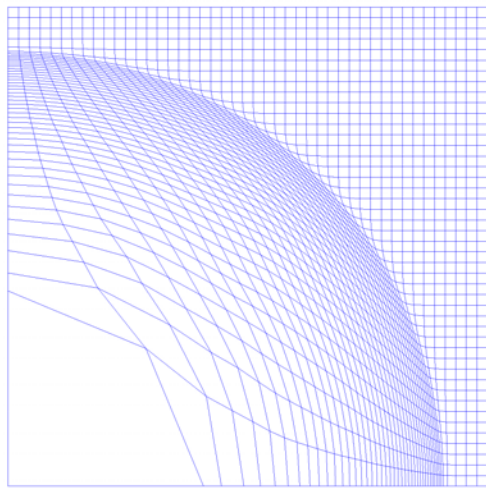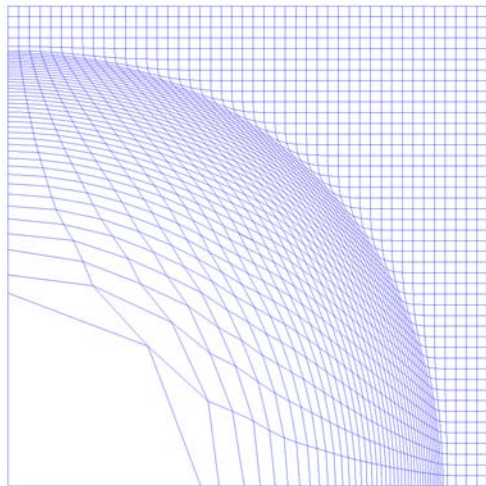
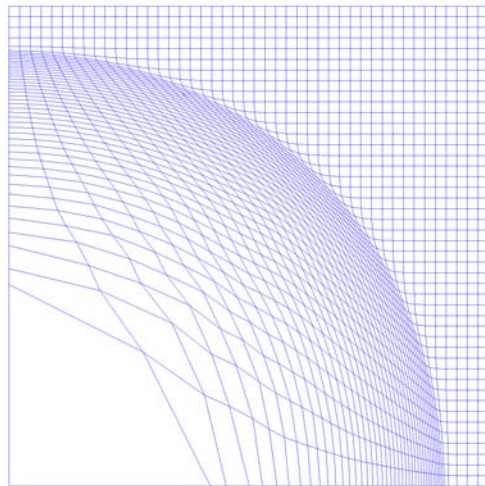(a) FB, single-point quadrature for $\boldsymbol{\sigma}_{art}$.
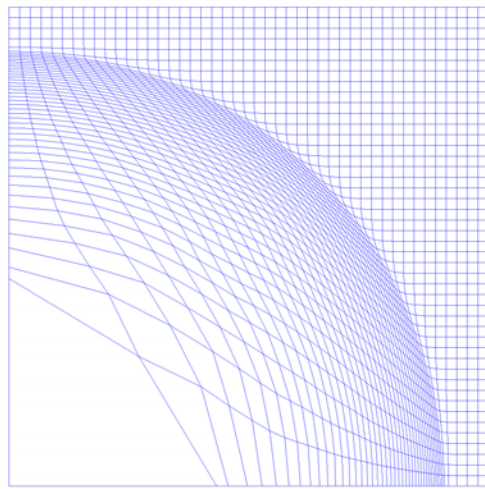
(b) FB, four-point quadrature for $\boldsymbol{\sigma}_{art}$.
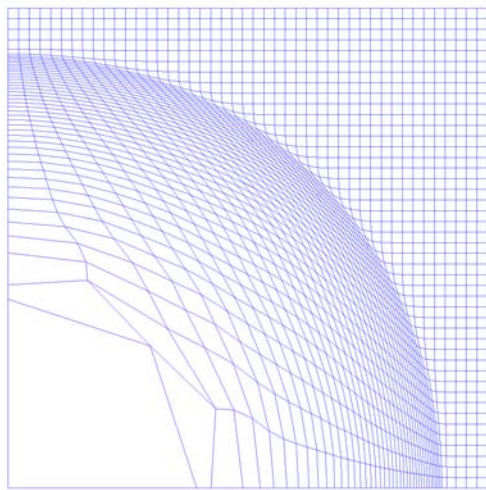
(c) VMS-I, single-point quadrature for $\boldsymbol{\sigma}_{art}$.
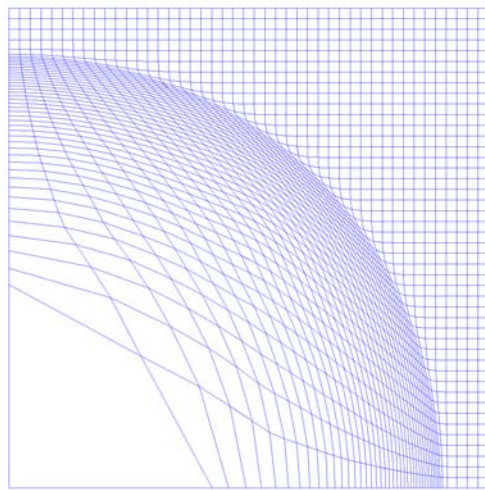
(d) VMS-I, four-point quadrature for $\boldsymbol{\sigma}_{art}$.

(e) VMS-II, single-point quadrature for $\boldsymbol{\sigma}_{art}$.

(f) VMS-II, four-point quadrature for $\boldsymbol{\sigma}_{art}$.

Figure 8. Two-dimensional Sedov test, comparison of the FB, VMS-I, and VMS-II stabilization approaches. Left column: Single-point integration for $\boldsymbol{\sigma}_{art}$. Right column: four-point integration for $\boldsymbol{\sigma}_{art}$.

(a) FB, $c_{FB} = 0.05$, $c_\tau = 7$.   (b) FB, $c_{FB} = 0.08$, $c_\tau = 7$.

(c) FB, $c_{FB} = 0.12$, $c_\tau = 7$.   (d) FB, $c_{FB} = 0.15$, $c_\tau = 7$.
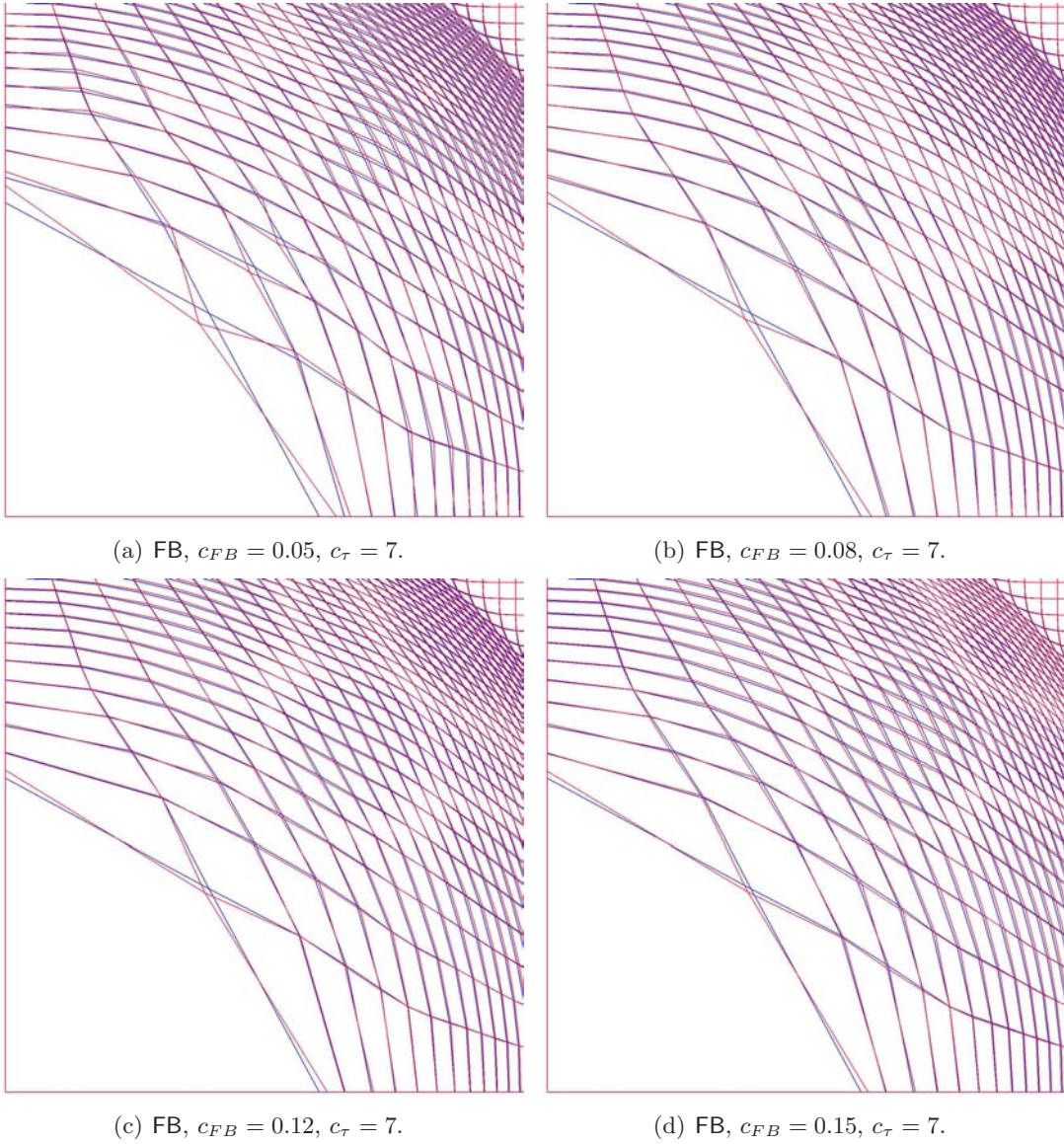
Figure 9. Two-dimensional Sedov test, zoomed view near the origin. Comparison of the VMS-I and FB stabilization approaches, for different value of the constant parameter in the FB hourglass viscosity. For all four pictures, FB in red, VMS-I in blue.

The six pictures composing Figure 8 show an interesting comparison between the effect of the VMS-I, VMS-II, and FB approaches in combination with different quadrature rules for the artificial viscosity. In particular, the effects of non-linear coupling between the artificial viscosity and the VMS-I stabilization term appear clear in Figure 8(c). The best result in terms of smoothness of the final grid configuration and absence of note-to-node oscillations is given by the VMS-I method with full integration of the shock-capturing term (Fig. 8(d)).

However, when the VMS-I method is combined with single-point quadrature, the mesh distortion increases considerably near the origin (Fig. 8(c)). For single-point quadrature, the VMS-II method offers superior results (Fig. 8(e)). However, when VMS-II is combined with full-quadrature, probably because of the incomplete definition of the pressure residual, the results are less accurate than for the VMS-I method.
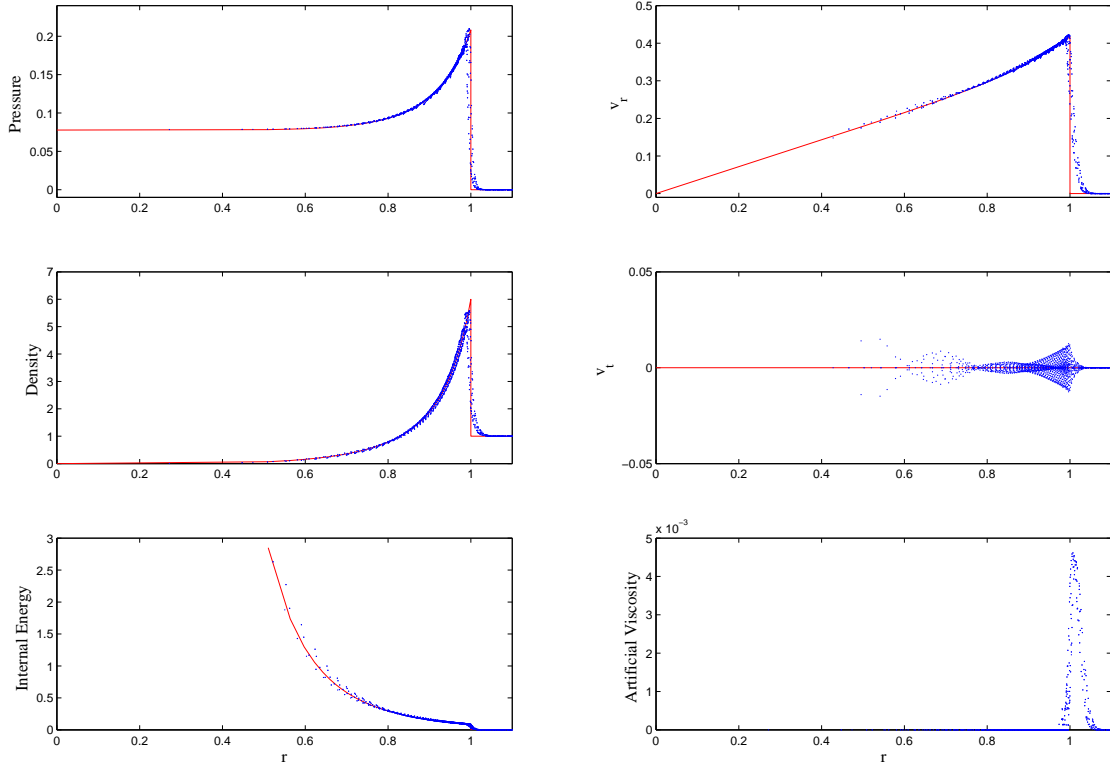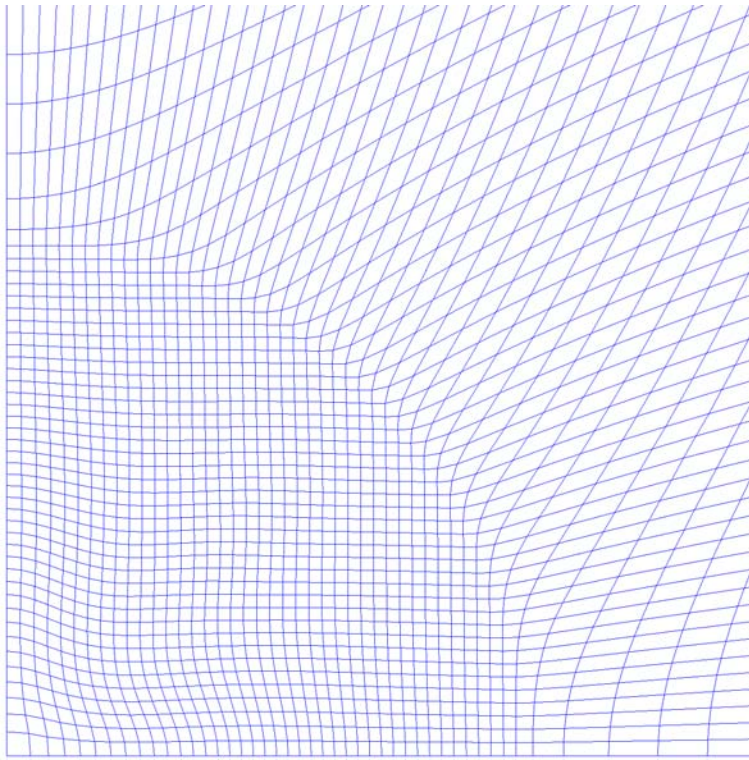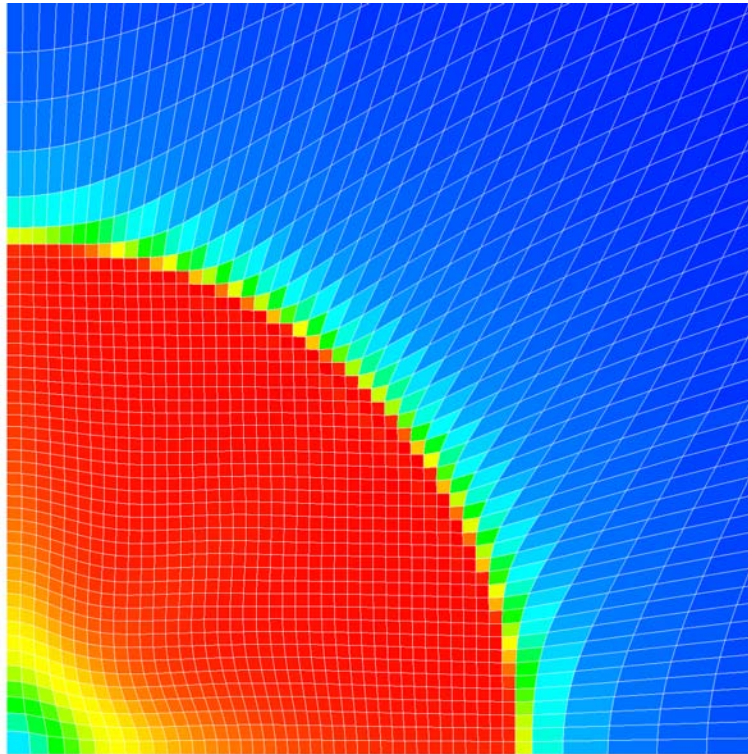
37

Figure 10. Two-dimensional Sedov test: Comparison with the exact solution. VMS-I with fully-integrated artificial viscosity. On the left column, from the top down: Pressure, density and internal energy. On the right column, from top down: Radial velocity v_r, tangential velocity v_t, and artificial viscosity ν_{art}. Each variable is plotted as a function of the radius $r = \sqrt{x_1^2 + x_2^2}$. All solution points are rotated around the origin to align on a single radial plane. Results in the case of single-point integration for the artificial viscosity only, and single-point integration for the entire stress tensor $\tilde{\boldsymbol{\sigma}}$ with Flanagan-Belytschko hourglass control are virtually identical.

Figures 8(a) and 8(b) show the results for the FB hourglass control and a constant $c_{FB} = 0.15$. The FB yields the best results with single-point quadrature integration, but it is somewhat inferior to the VMS-I method when full integration is performed. To see more clearly this last point, Figure 9 shows a comparison of the VMS-I and the FB approaches, as the constant in the FB viscosity spans the interval $[0.05, 0.15]$. For low values of c_{FB}, an hourglass pattern, originating in the large element in the lower left corner of the domain, is clearly visible in Figure 9(a). As the the constant c_{FB} is increased (see Figs. 9(b), 9(c), and 9(d)), the hourglass pattern, although increasingly more damped, persists.

(a) Mesh deformation.

(b) Density color plot.

Figure 11. Two-dimensional Noh test on a Cartesian mesh, VMS-I with fully-integrated artificial viscosity.
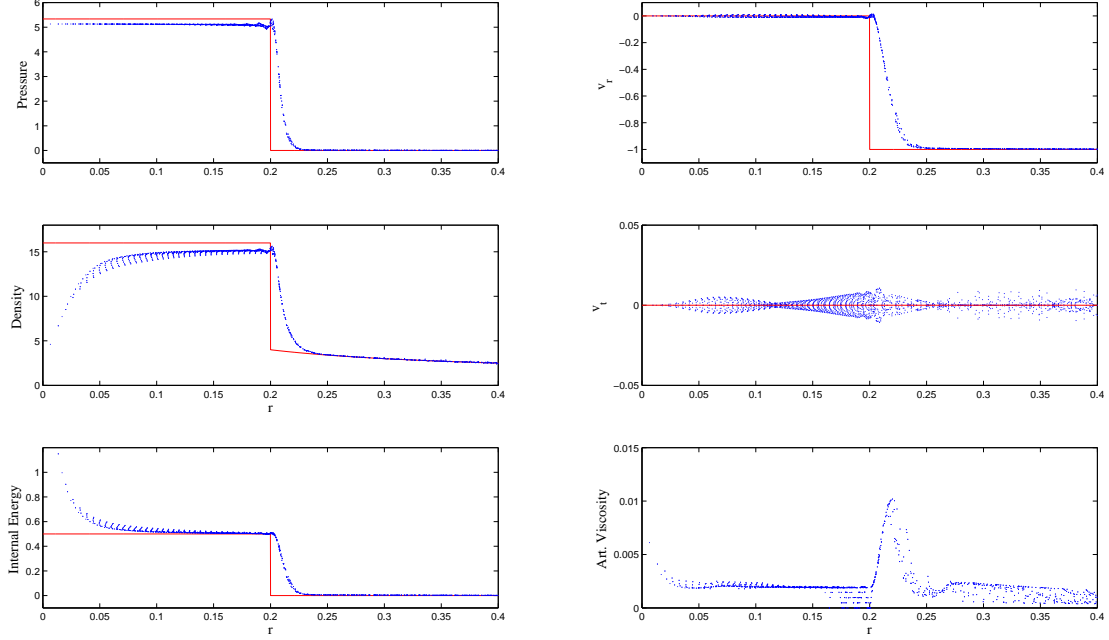
Figure 12. Two dimensional Noh test: Comparison with the exact solution. VMS-I with fully-integrated artificial viscosity. On the left column, from the top down: Pressure, density and internal energy. On the right column, from top down: Radial velocity v_r, tangential velocity v_t, and artificial viscosity ν_{art}. Each variable is plotted as a function of the radius $r = \sqrt{x_1^2 + x_2^2}$. All solution points are rotated around the origin to align on a single radial plane.

Quantitative comparison between the VMS-I approach and the exact solution to the Sedov problem are shown in Figure 10: When full integration is applied, the VMS-II and FB yield very similar results. It is worthwhile to notice the peak of the density value at approximately 5.5, against the exact value of 6.0. This is a very accurate result, considering the coarseness of the initial mesh. In the proposed test perfect cylindrical symmetry is not expected, since, due to the geometry of the mesh and initial/boundary conditions, the geometrical axis of symmetry is the bi-secant of the quadrant. Notice then the perfectly mirrored pattern in the solution for the tangential component of the velocity.
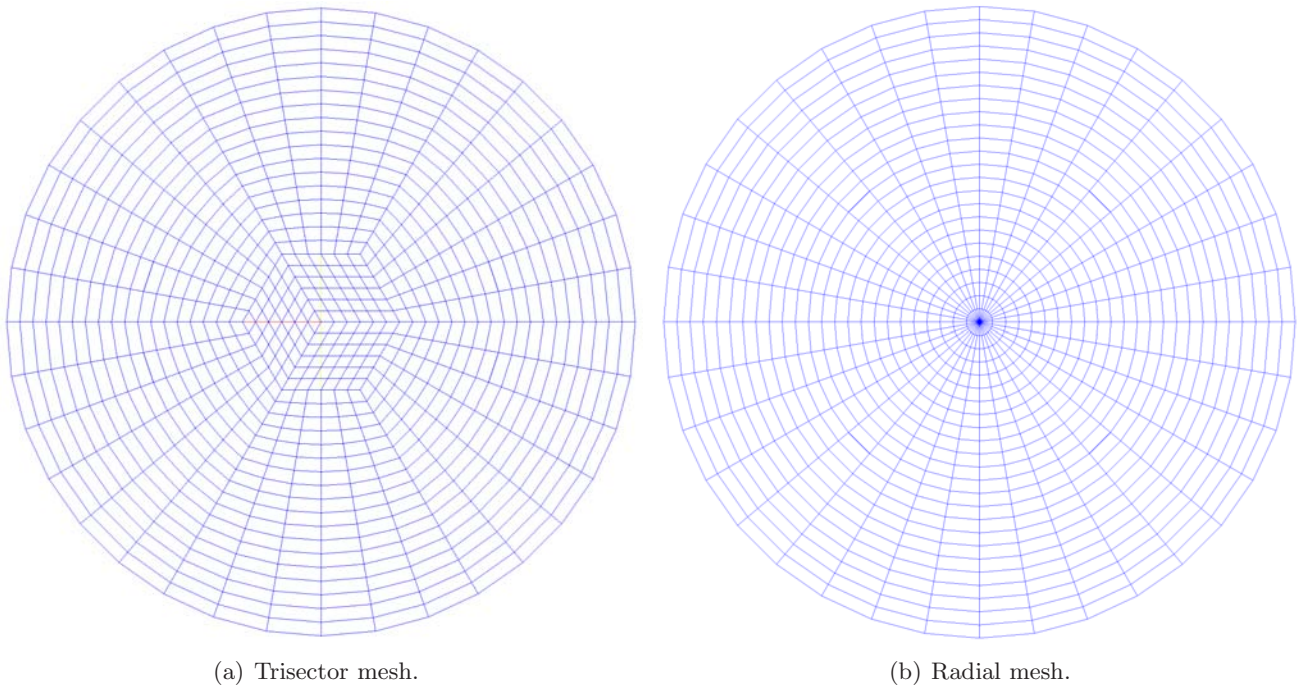
(a) Trisector mesh.　　　　　　　　　(b) Radial mesh.

Figure 13. Two-dimensional Noh test on a radial trisector mesh. The initial mesh is given by an hexagonal pattern at the center, with a transition to a radially symmetric pattern towards the outside boundary, as shown in Figure 13(a). The mesh is composed of three identical sectors, rotated by 120 and 240 degrees with respect to one another. Figure 13(b) presents a radially symmetric mesh, composed of 36 elements along the circumference, and 24 along the radius, which is used to generate a reference solution.

8.4 Noh test in two dimensions

The Noh [28] test is an implosion test. The velocity has an initial uniform radial distribution (the velocity field points to the origin, and has unit magnitude, except at the origin, where it is forced to zero).

The initial energy should be zero, but for practical purposes the value 10^{-14} is used. The constant $\gamma = 5/3$ is applied to all computations. The exact solution for the density behind the shock is 16.0 and decays as $1 + t/r$ in front of the shock, where t is time and $r = \sqrt{x_1^2 + x_2^2}$ is the radius. The pressure past the shock takes the value $16/3$. The shock speed is $1/3$, so that at the final time of 0.6 in the computation, the discontinuity is found at $r = 0.2$.

8.4.1 Noh test on a Cartesian quadrant

Similarly to the case of the Sedov test, a Cartesian quadrant $[0, 1] \times [0, 1]$ is initially subdivided into 50×50 squares. Mesh deformation and density color plots are presented in Figure 11: The smoothness of the shocked grid is appreciable. Comparison with the exact solution are presented in Figure 12. The results show smoothness in all variables, and values of the plateaus for the density and pressure are in good agreement with the exact solution, considering the coarseness of the mesh (for extensive studies on this problem, see, e.g., [28]).
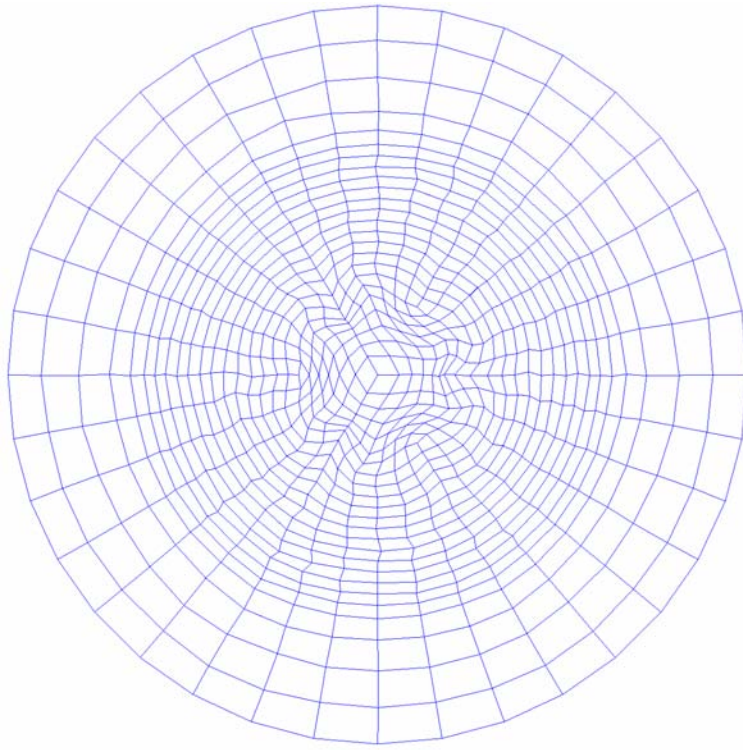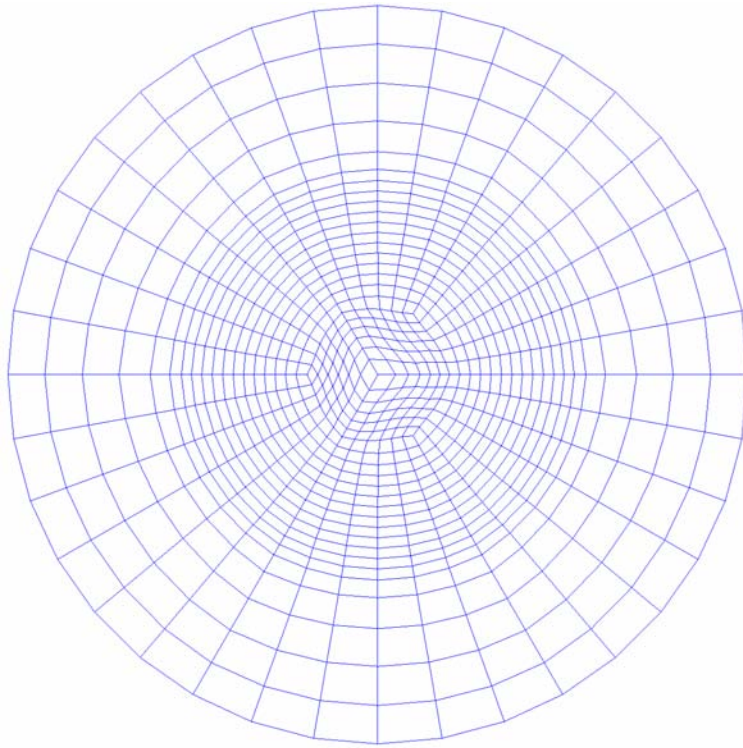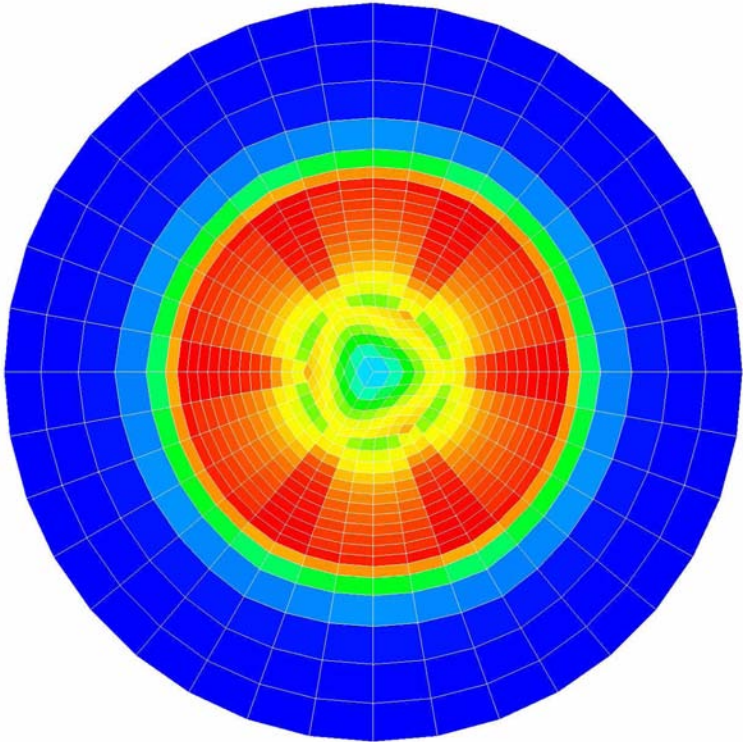
(a) Mesh deformation.
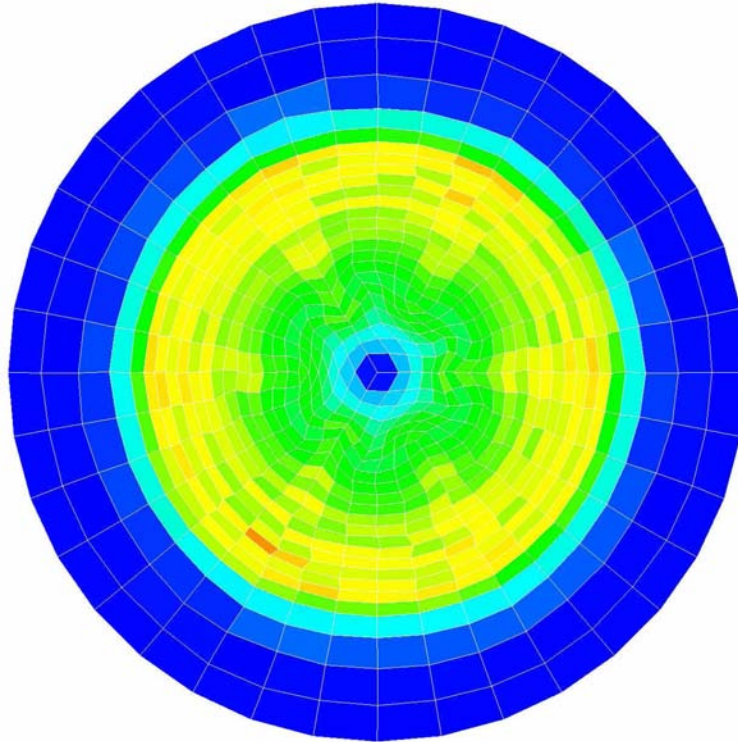
(b) Density color plot.

Figure 14. Two-dimensional Noh test on the trisector mesh. FB with the artificial stress tensor $\boldsymbol{\sigma}_{art}$ defined as in (138).

(a) Mesh deformation.

(b) Density color plot.

Figure 15. Two-dimensional Noh test on the trisector mesh. VMS-I with the artificial stress tensor $\boldsymbol{\sigma}_{art}$ is defined as in (137). Very similar results are obtained with FB.
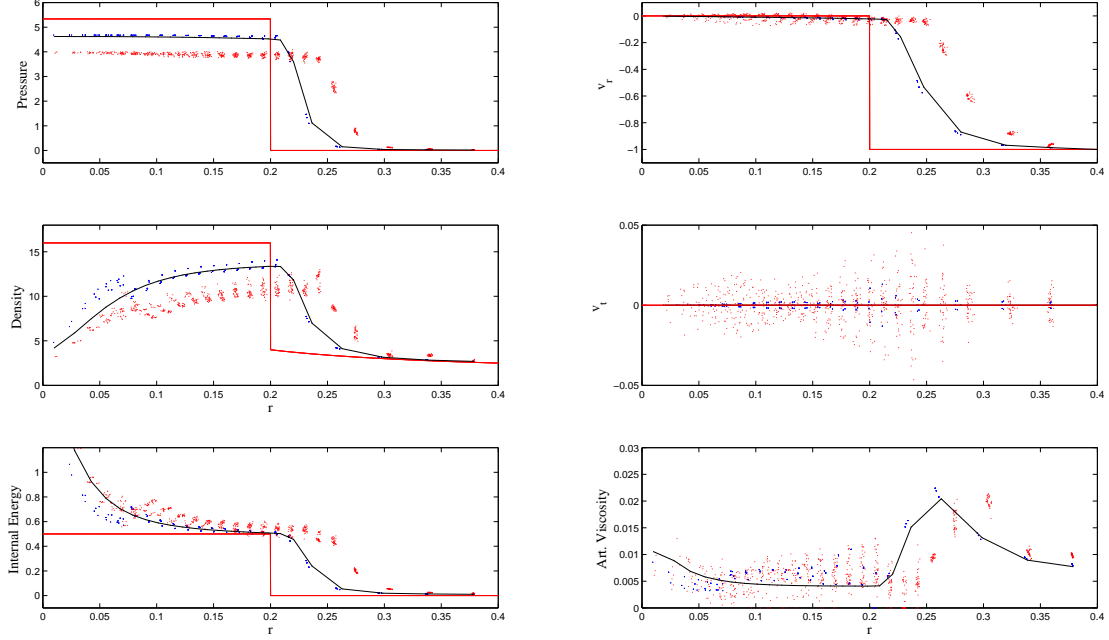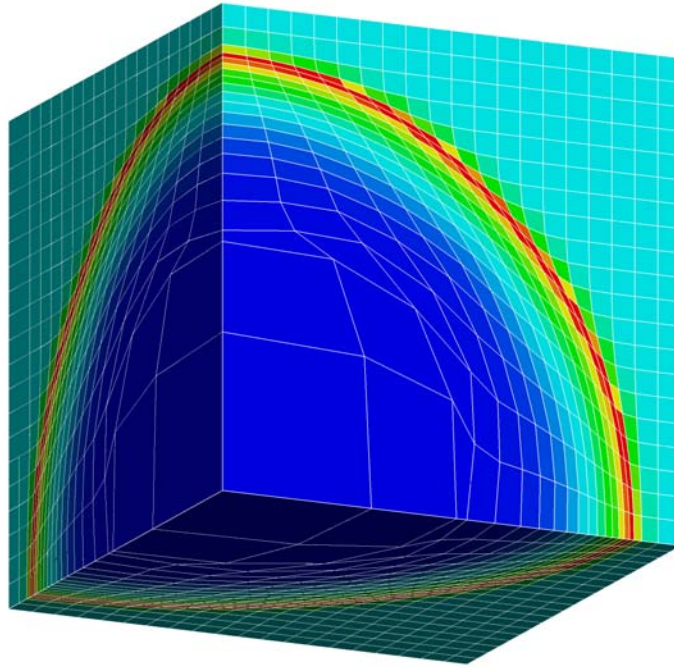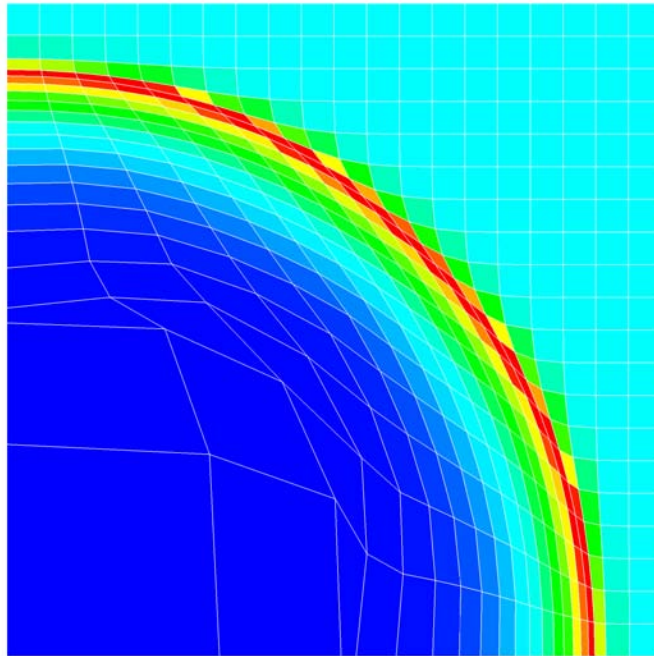
Figure 16. Two-dimensional Noh test: Comparison with the exact solution (continuous red curve) of the results of Figure 14 (red dots) and Figure 15 (blue dots). The continuous black line represents the solution on the radially symmetric mesh of Figure 13(b), using the tensor artificial viscosity (137). The components of the solution are presented as in Figure 12.

8.4.2 Noh test on a mesh with trisector symmetry

From this variant of the two-dimensional Noh test, very important conclusions can be drawn on some aspects of the artificial viscosity implementation. In particular, this is an interesting test for comparing the performance of $\boldsymbol{\sigma}_{art}$ as defined in (137) with respect to more classical definition (138). Due to the initial node configuration (see Fig. 13(a)), the shocked mesh tends to produce homogenous shear modes along the secant lines at 0, 120, and 240 degrees. Shear-induced, "jet-like" patterns can be clearly seen in Figure 14. The hourglass control is no help in this case, since pure shear motion is point-wise divergence-free, and two-dimensional hourglass modes are not divergence-free. The situation is much improved in the case when the artificial stress $\boldsymbol{\sigma}_{art}$ is defined according to (137). As can be seen in Figure 15, shear motion is appropriately damped in the shock layer, and does not propagate to the rest of the flow. Consequently, mesh smoothness, and the accuracy of the solution are much improved (see Fig. 15).

(a) Perspective view.

(b) Side view from the x_1-axis.

Figure 17. Three-dimensional Sedov test, VMS-I approach, density contour plots.
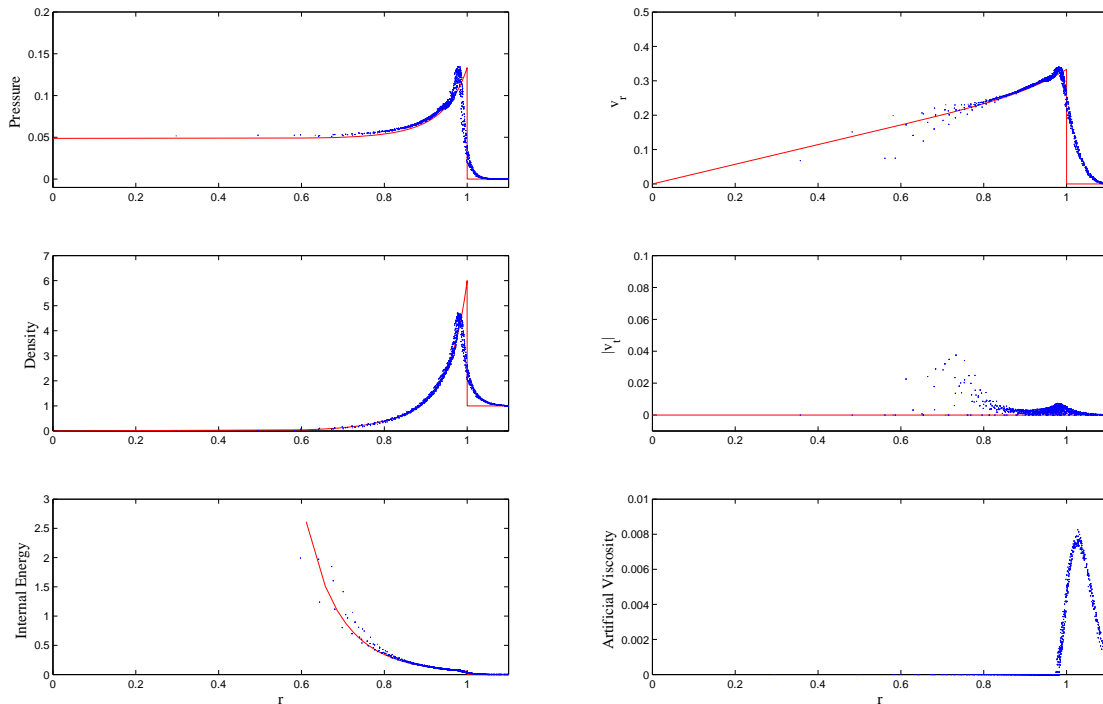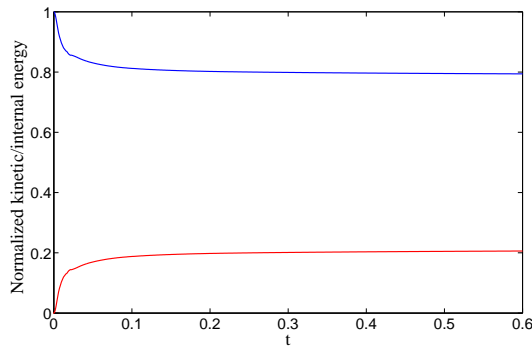
Figure 18. Three-dimensional Sedov test: Comparison between the VMS-I approach and the exact solution. On the left, from the top down: Pressure, density and internal energy. On the right, from top down: Radial velocity v_r, tangential velocity v_t, and artificial viscosity ν_{art}. Each variable is plotted as a function of the radius $r = \sqrt{x_1^2 + x_2^2 + x_3^2}$.

Notice in Figure 16 the large errors in the solution plateaus and arrival time of the shock wave when the pressure-like artificial viscosity operator (138) is used. By contrast, the solution for the tensor artificial viscosity (137) is much improved, and significantly closer to the reference numerical solution on the radial mesh of Figure 13(b).

8.5 Sedov test in three dimensions

The Sedov test in three dimensions is much more challenging than its two-dimensional counterpart, due to the increased distortion undergone by the elements. The proposed version of the Sedov blast test is performed on the $[0, 1.1] \times [0, 1.1] \times [0, 1.1]$ octant, subdivided into $20 \times 20 \times 20$ cubes. The initial density has a uniform unit distribution. The value $\gamma = 1.4$ was used. The simulations are performed at $CFL = 0.5$. For FB, VMS-I, and VMS-II, it was not possible to successfully run to completion computations in which the initial condition for the energy involved concentrating all the initial internal energy in one cell of the mesh. Therefore, a "mitigated" initial condition for the internal energy is adopted, in which nodal projection followed by cell averaging redistributed the initial energy over eight corner cells rather than one. Indicating with the triplet $(i, j, k) = (0, 0, 0)$ the corner cell where the internal energy $e_0 = 639.4$ had to

(a) Normalized kinetic/internal energies.
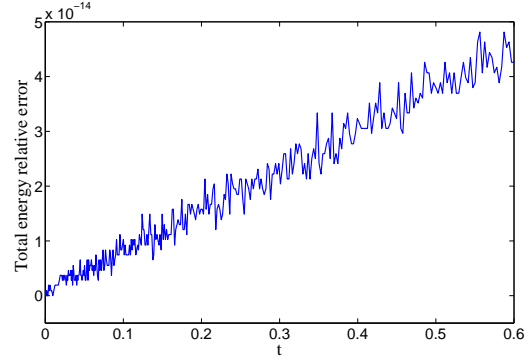
(b) Total energy relative error.

Figure 19. Energy history for the three-dimensional Sedov test. Figure 19(a) shows the time history of the kinetic (red) and internal (blue) energies, normalized with respect to the initial total energy, $\mathcal{E}_0^{tot}$. Figure 19(b) shows the time history of the relative error on the total energy $(\mathcal{E}^{tot}(t) - \mathcal{E}_0^{tot})/\mathcal{E}_0^{tot}$. Notice that the scale of the vertical axis is multiplied by 10^{-14}.

be originally concentrated, the following initial energy distribution was adopted:

$$e_{(0,0,0)} = \frac{27}{64}e_0 \ , \tag{155}$$

$$e_{(1,0,0)} = e_{(0,1,0)} = e_{(0,0,1)} = \frac{9}{64}e_0 \ , \tag{156}$$

$$e_{(1,1,0)} = e_{(0,1,1)} = e_{(1,0,1)} = \frac{3}{64}e_0 \ , \tag{157}$$

$$e_{(1,1,1)} = \frac{1}{64}e_0 \ , \tag{158}$$

where, for example, the subscript $(1,0,0)$ indicates the cell next to the corner cell along the x_1 direction. The internal energy is set to "zero" (actually 10^{-14}) everywhere else in the initial domain. Results are shown in Figure 17 and Figure 18 for the VMS-II case. Similar results have been obtained with the FB approach, but with a constant $c_{FB} = 0.25$, considerably higher than the suggested range of values. It is also important to notice that this choice of the constant is not appropriate for the three-dimensional Noh test documented below, for which the constant c_{FB} had to be reduced to values in the interval $[0.05, 0.075]$. This suggests that, the practice of not separating the physical from the artificial components of the hourglass control – as is usually done in the extensions of the FB approach to fluids – may endanger robustness. To be more specific, the Flanagan-Belytschko hourglass control was originally intended for solids, and only at a later stage was applied to fluid computations. In the case of a solid, applying an hourglass viscosity to both the $\mathcal{H}_{div}$ and $\mathcal{H}_{shear}$ modes is a very sensible choice, since the material possesses shear strength. But for a fluid, the modes in $\mathcal{H}_{div}$ have a physical significance, while the modes in $\mathcal{H}_{shear}$ are pure artifacts of the element technology. Therefore, the variational multi-scale approach seems to offer a pathway for increased robustness in hourglass control.
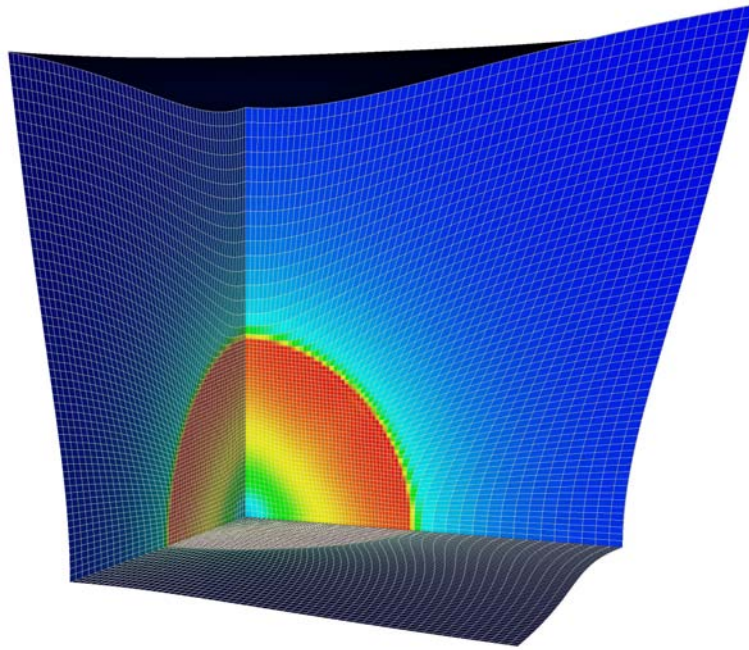
(a) Perspective view.
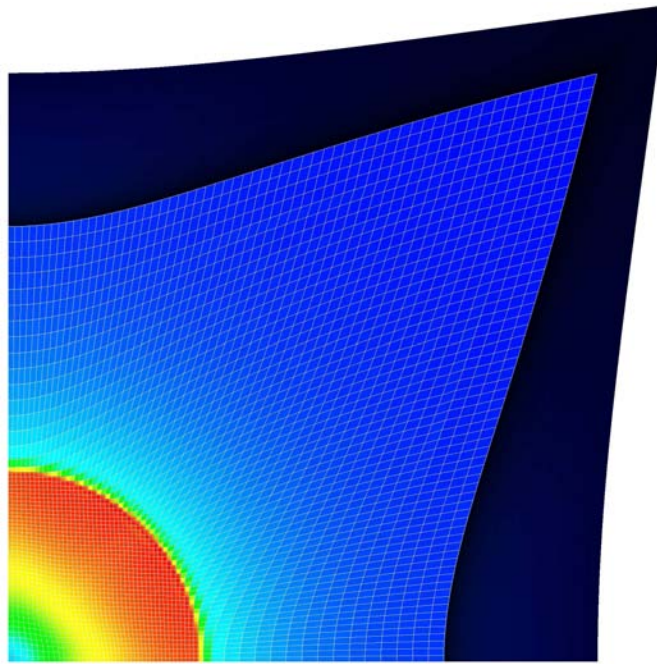
(b) Side view from the x_1-axis.

Figure 20. Three-dimensional Noh test on the 60^3 mesh, VMS-I approach, density contour plots.
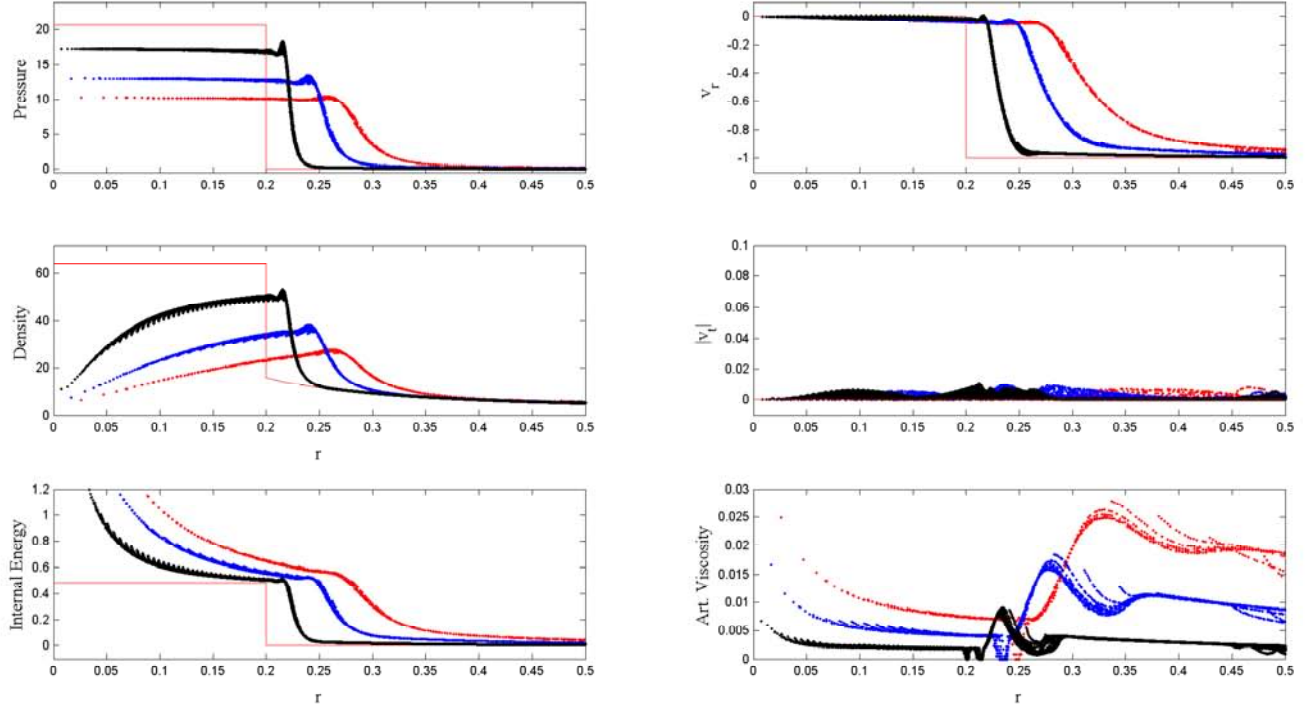
Figure 21. Three-dimensional Noh test: Comparison with the exact solution for the 20^3 (red), 30^3 (blue), and 60^3 (black) meshes. VMS-I with fully-integrated artificial viscosity. On the left column, from the top down: Pressure, density and internal energy. On the right column, from top down: Radial velocity v_r, tangential velocity v_t, and artificial viscosity ν_{art}. Each variable is plotted as a function of the radius $r = \sqrt{x_1^2 + x_2^2 + x_3^2}$.

Figure 18 shows somewhat less accurate results than Figure 10. This may be due to the coarseness of the mesh, also in conjunction to the modifications applied to the initial conditions, and the three-dimensional nature of the solution. Figure 19(a) shows the time-history of the total kinetic energy and the total internal energy, normalized with respect to the initial total energy, $\mathcal{E}_0^{tot} = \mathcal{E}^{tot}(t_0)$. Given the imposed boundary conditions, the total energy must be conserved throughout the computation. Figure 19(b) shows that the relative error in the total energy is on the order of 10^{-14}, well within the machine precision.

8.6   Noh test in three dimensions

The initial conditions for the Noh test in three dimensions are analogous to the two-dimensional case: In three dimension, the initial velocity vector field is of unit magnitude and points to the origin of the reference frame, while the thermodynamic variables have the same initial conditions as in the two-dimensional case. The domain $[0, 1.1] \times [0, 1.1] \times [0, 1.1]$ is uniformly meshed with three meshes of resolution $20 \times 20 \times 20$, $30 \times 30 \times 30$, and $60 \times 60 \times 60$ cubes. The exact solution for the density behind the shock is 64.0 and decays as $(1 + t/r)^2$ in front of the shock, where t is time and $r = \sqrt{x_1^2 + x_2^2 + x_3^2}$ is the radius. The pressure past the shock takes the value 62/3. The shock speed is 1/3, so that at the final time of 0.6 in the computation, the discontinuity is found at $r = 0.2$.

Only results for VMS-I are presented, in Figures 20 and 21. Similar results can be obtained with FB, but, as already mentioned, to avoid volume inversions near the origin, the constant c_{FB} has to be reduced to values in the range $[0.05, 0.075]$. Because the plateaus of the density and pressure at at much higher values than in the two-dimensional case, even a resolution of 60^3 elements is still coarse to fully capture the solution. In Figure 21, it can be appreciated the convergence of the numerical to the exact solution, as the mesh is refined. These results are in very good agreement with the one-dimensional, spherically-symmetric solution, computed in [28] using $50 - 70$ radial zones. As mentioned in [28], an acceptable resolution for this problem would be 100 radial zones, roughly equivalent to $100 \times 100 \times 100$ cartesian cells. This would require a numerical computation of one million elements, a task beyond the scope of the present work.

9   Summary

A novel multi-scale method for Lagrangian shock hydrodynamics has been presented. The formulation of the proposed method in the context of Q1/P0 finite elements makes it widely applicable to state-of the-practice hydrodynamic algorithms.

The proposed method builds on a mid-point time integrator implemented as a conservative predictor/multicorrector scheme. The stabilization augments the original Galerkin formulation without perturbing its global conservation properties.

The multi-scale approach leads to a consistent method, in which instabilities (typically, of hourglass type) are controlled by the stabilizing effect of an appropriate pressure residual.

By rational thermodynamic arguments, it has been shown that the pressure residual is tied to the Clausius-Duhem inequality, and, effectively, measures the creation of entropy due to instabilities in the numerical discretization. These arguments imply the physical consistency of the multi-scale stabilization. Connections with previous work on physical hourglass stabilization have been drawn. However, the proposed approach takes the discussion to a new level, since, in past developments, many aspects of the interplay between physics and numerics have been overlooked.

In the case of three-dimensional flows, the addition of a hourglass viscosity aimed at damping divergence-free, non-homogeneous shear is necessary. This pinpointed a major disadvantage in fluid computations of the Q1/P0 element technology, which requires stabilization of fine-scale shear modes, although inviscid fluids have no shear-strength or shear-damping mechanisms. In this context, the multi-scale analysis provides a new perspective, and allows for a more flexible design of hourglass viscosities aimed at damping such hourglass instabilities.

Numerical results in two and three dimensions in the case of compressible gas dynamics show that the method has comparable and in some cases superior performance to state-of-the-practice techniques for hourglass control.

More work is needed to fully investigate the robustness and accuracy properties of the proposed method, and extend it to more complex computations, involving multiple materials, or multiple-physics. Of great importance is also the extension of the proposed multi-scale approach to solids. In this case, the multi-scale approach should provide the full stabilization mechanism for Q1/P0 formulations, since the material possess shear strength, and additional fine-scale shear control mechanisms should not be required.

References

[1] S. S. Antman. *Nonlinear problems of elasticity*, volume 107 of *Applied mathematical sciences*. Springer, New York, 2nd edition, 2005.

[2] T. Belytschko and L. P. Bindeman. Assumed strain stabilization of the 4-node quadrilateral with 1-point quadrature for nonlinear problems. *Computer Methods in Applied Mechanics and Engineering*, **88**(3):311–340, 1991.

[3] T. Belytschko and L. P. Bindeman. Assumed strain stabilization of the eight node hexahedral element. *Computer Methods in Applied Mechanics and Engineering*, **105**(2):225–260, 1993.

[4] T. Belytschko, W. K. Liu, and B. Moran. *Nonlinear Finite Elements for Continua and Structures*. J. Wiley & Sons, New York, 2000.

[5] D. J. Benson. Computational methods in Lagrangian and Eulerian hydrocodes. *Computer Methods in Applied Mechanics and Engineering*, **99**:235–394, 1992.

[6] E. J. Caramana, M. J. Shashkov, and P. P. Whalen. Formulations of artificial viscosity for multi-dimensional shock wave computations. *Journal of Computational Physics*, **144**:70–97, 1998.

[7] D. E. Carlson. Linear thermoelasticity. In C. A. Truesdell, editor, *Mechanics of Solids*, volume II, chapter 2, pages 297–345. Springer-Verlag, New York, 1984.

[8] M. A. Christon. Pressure gradient approximations for staggered-grid finite element hydrodynamics. *International Journal for Numerical Methods in Fluids*, 2005. In preparation.

[9] R. Codina, J. Principe, O. Guash, and S. Badia. Time dependent subscales in the stabilized finite element approximation of incompressible flow problems, 2006. Submitted.

[10] B. D. Coleman and V. J. Mizel. Existence of caloric equations of state in thermodynamics. *The Journal of Chemical Physics*, **40**(4):1116–1125, 1964.

[11] D. P. Flanagan and T. Belytschko. A uniform strain hexahedron and quadrilateral with orthogonal hourglass control. *International Journal for Numerical Methods in Engineering*, **17**(5):679–706, 1981.

[12] G. L. Goudreau and J. O. Hallquist. Recent developments in large-scale finite element Lagrangian hydrocode technology. *Computer Methods in Applied Mechanics and Engineering*, **33**(1-3):725–757, September 1982.

[13] J. O. Hallquist. LS-DYNA theory manual. Technical report, Livermore Software Technology Corporation, Livermore, CA, March 2006. Available at: `http://www.lstc.com`.

[14] G. Hauke. Simple stabilizing matrices for the computation of compressible flows in primitive variables. *Computer Methods in Applied Mechanics and Engineering*, **190**:6881–6893, 2001.

[15] G. Hauke and T. J. R. Hughes. A unified approach to compressible and incompressible flows. *Computer Methods in Applied Mechanics and Engineering*, **113**:389–396, 1994.

[16] G. Hauke and T. J. R. Hughes. A comparative study of different sets of variables for solving compressible and incompressible flows. *Computer Methods in Applied Mechanics and Engineering*, **153**:1–44, 1998.

[17] T. J. R. Hughes. *The Finite Element Method: Linear Static and Dynamic Finite Element Analysis*. Prentice-Hall, Englewood Cliffs, New Jersey, 1987. (Dover reprint, 2000).

[18] T. J. R. Hughes. Multiscale phenomena: Green's functions, the Dirichlet-to-Neumann formulation, subgrid-scale models, bubbles and the origin of stabilized methods. *Computer Methods in Applied Mechanics and Engineering*, **127**:387–401, 1995.

[19] T. J. R. Hughes, G.R. Feijóo, L. Mazzei, and J.-B. Quincy. The Variational Multiscale Method — a paradigm for computational mechanics. *Computer Methods in Applied Mechanics and Engineering*, **166**:3–24, 1998.

[20] T. J. R. Hughes, L. P. Franca, and G. M. Hulbert. A new finite element formulation for computational fluid dynamics: VIII. The Galerkin/least-squares method for advective-diffusive equations. *Computer Methods in Applied Mechanics and Engineering*, **73**:173–189, 1989.

[21] T. J. R. Hughes, L. P. Franca, and M. Mallet. A new finite element formulation for computational fluid dynamics: VI. Convergence analysis of the generalized SUPG formulation for linear time-dependent multidimensional advective-diffusive systems. *Computer Methods in Applied Mechanics and Engineering*, **63**:97–112, 1987.

[22] T. J. R. Hughes and M. Mallet. A new finite element formulation for computational fluid dynamics: III. The generalized streamline operator for multidimensional advective-diffusive systems. *Computer Methods in Applied Mechanics and Engineering*, **58**:305–328, 1986.

[23] T. J. R. Hughes, M. Mallet, and A. Mizukami. A new finite element formulation for computational fluid dynamics: II. Beyond SUPG. *Computer Methods in Applied Mechanics and Engineering*, **54**:341–355, 1986.

[24] T. J. R. Hughes, G. Scovazzi, and Franca L.P. Multiscale and stabilized methods. In E. Stein, R. de Borst, and T. J. R. Hughes, editors, *Encyclopedia of Computational Mechanics*. John Wiley & Sons, 2004.

[25] T. J. R. Hughes and T. E. Tezduyar. Finite element methods for first-order hyperbolic systems with particular emphasis on the compressible Euler equations. *Computer Methods in Applied Mechanics and Engineering*, **45**:217–284, 1984.

[26] V. F. Kuropatenko. On difference methods for the equations of hydrodynamics. In N. N. Janenko, editor, *Difference methods for solutions of problems of mathematical physics, I*. American Mathematical Society, Providence, RI, 1967.

[27] A. Masud. Effects of mesh motion on the stability and convergence of ALE based formulations for moving boundary flows. *Computational Mechanics*, DOI:10.1007/s00466–006–0062–9 (to appear), 2006.

[28] W. F. Noh. Errors for calculations of strong shocks using an artificial viscosity and an artificial heat flux. *Journal of Computational Physics*, **72**:78–120, 1987.

[29] M. A. Puso. A highly efficient enhanced assumed strain physically stabilized hexahedral element. *International Journal for Numerical Methods in Engineering*, **49**(8):1029–1064, November 2000.

[30] G. Scovazzi. Stabilized shock hydrodynamics: II. Design and physical interpretation of the SUPG operator for Lagrangian computations. *Computer Methods in Applied Mechanics and Engineering*, **196**(4–6):966–978, 2007.

[31] G. Scovazzi, M. A. Christon, T. J. R. Hughes, and J. N. Shadid. Stabilized shock hydrodynamics: I. A Lagrangian method. *Computer Methods in Applied Mechanics and Engineering*, **196**(4–6):923–966, 2007.

[32] L. I. Sedov. *Similarity and Dimensional Methods in Mechanics.* Academic Press, New York, 1959.

[33] F. Shakib, T. J. R. Hughes, and Z. Johan. A new finite element formulation for computational fluid dynamics: X. The compressible Euler and Navier-Stokes equations. *Computer Methods in Applied Mechanics and Engineering*, **89**:141–219, 1991.

[34] J. C. Simo and T. J. R. Hughes. *Computational Inelasticity.* Springer, New York, 1998.

[35] J. C. Simo and N. Tarnow. The discrete energy-momentum method. Conserving algorithms for non-linear elastodynamics. *Zeitschrift für Angewandte Mathematik und Physik (ZAMP)*, **43**(5):757–792, September 1992.

[36] T. E. Tezduyar. Stabilized finite element formulations for incompressible flow computations. *Advances in Applied Mechanics*, **28**:1–44, 1992.

[37] T. E. Tezduyar. Computation of moving boundaries and interfaces and stabilization parameters. *International Journal for Numerical Methods in Fluids*, **43**:555–575, 2003.

[38] T. E. Tezduyar. Finite element methods for fluid dynamics with moving boundaries and iterfaces. In E. Stein, R. de Borst, and T. J. R. Hughes, editors, *Encyclopedia of Computational Mechanics.* John Wiley & Sons, 2004.

[39] T. E. Tezduyar, M. Behr, and J. Liou. A new strategy for finite element computations involving moving boundaries and interfaces – The deforming-spatial-domain/space-time procedure: I. The concept and the preliminary numerical tests. *Computer Methods in Applied Mechanics and Engineering*, **94**:339–351, 1992.

[40] T. E. Tezduyar, M. Behr, S. Mittal, and J. Liou. A new strategy for finite element computations involving moving boundaries and interfaces – The deforming-spatial-domain/space-time procedure: II. Computation of free-surface flows, two-liquid flows, and flows with drifting cylinders. *Computer Methods in Applied Mechanics and Engineering*, **94**:353–371, 1992.

[41] T. E. Tezduyar, S. Mittal, S. E. Ray, and R. Shih. Incompressible flow computations with stabilized bilinear and linear equal-order-interpolation velocity-pressure element. *Computer Methods in Applied Mechanics and Engineering*, **95**:221–242, 1992.

[42] T. E. Tezduyar and M. Senga. Stabilization and shock-capturing parameters in SUPG formulation of compressible flows. *Computer Methods in Applied Mechanics and Engineering*, **195**:1621–1632, 2006.

[43] C. A. Truesdell. *Rational thermodynamics.* Springer-Verlag, New York, 2nd edition, 1984.

[44] C. A. Truesdell and W. Noll. *The non-linear field theories of mechanics.* Springer-Verlag, New York, 2nd edition, 1992.

[45] F. Van der Ween and T. Belytschko. Correction of article by D. P. Flanagan and T. Belytschko. *International Journal for Numerical Methods in Engineering*, **19**(3):467–468, 1983.

DISTRIBUTION:

1 Thomas J. R. Hughes
ICES, U. Texas at Austin
1 University Station C0200
Austin, TX 78712-0027

1 Mikhail Shashkov
Theoretical Division, Group T7
LANL, MS-B284
Los Alamos, New Mexico 87545

1 MS 1319
   Pavel Bochev, 1414

1 MS 1319
   S. Scott Collis, 1414

1 MS 0380
   Martin Heinstein, 1542

1 MS 1319
   Edward Love, 1431

1 MS 1319
   Richard Lehoucq, 1414

1 MS 0378
   William Rider, 1431

1 MS 0378
   Allen Robinson, 1431

1 MS 1319
   Guglielmo Scovazzi, 1431

1 MS 0316
   John Shadid, 1437

1 MS 0382
   James Stewart, 1543

1 MS 0378
   Randall Summers, 1431

1 MS 0378
   Michael Wong, 1431

2 MS 9018
   Central Technical Files, 8944

2 MS 0899
   Technical Library, 4536